

Phase Transitions in Low-Dimensional Layered Double Perovskites: The Role of the Organic Moieties

Beatriz Martín-García^{†,‡,,}, Davide Spirito^{†,‡,*,}, Giulia Biffi^{†,¶}, Sergey Artyukhin[†], Francesco Bonaccorso^{†,#}, Roman Krahne[†].*

[†]Istituto Italiano di Tecnologia, Via Morego 30, 16163 Genova (Italy)

[‡]CIC nanoGUNE, Tolosa Hiribidea, 76, 20018 Donostia-San Sebastian, Basque Country (Spain)

[¶]IHP–Leibniz-Institut für innovative Mikroelektronik, Im Technologiepark 25, 15236 Frankfurt (Oder) (Germany)

[¶]Dipartimento di Chimica e Chimica Industriale, Università degli Studi di Genova, Via Dodecaneso 31, 16146 Genova (Italy)

[#]BeDimensional S.p.A., Via Lungotorrente secca 3d, 16163 Genova (Italy)

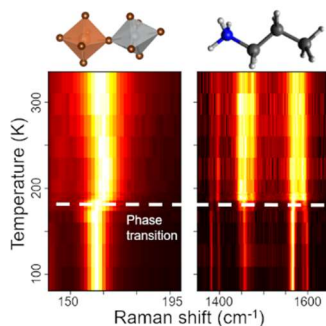
AUTHOR INFORMATION

Corresponding Author

*Beatriz Martín-García (b.martingarcia@nanogune.eu) and Davide Spirito (spirito@ihp-microelectronics.com)

ABSTRACT. Halide double perovskites are an interesting alternative to Pb-containing counterparts as active materials in optoelectronic devices. Low-dimensional double perovskites are fabricated by introducing large organic cations, resulting in organic/inorganic architectures with one or more inorganic octahedral layers separated by organic cations. Here, we synthesize layered double perovskites based on 3D $\text{Cs}_2\text{AgBiBr}_6$ that consist of double (2L) or single (1L) inorganic octahedral layers, using ammonium cations of different size and chemical structure. Temperature-dependent Raman spectroscopy reveals phase transition signatures in both inorganic lattice and organic moieties by detecting variations in their vibrational modes. Changes in the conformational arrangement of the organic cations to an ordered state coincide with a phase transition in the 1L systems with the shortest ammonium moieties. Significant changes of photoluminescence intensity observed around the transition temperature suggest that optical properties may be deeply affected by the octahedral tilts emerging at the phase transition.

TOC GRAPHICS



In the last years, metal-halide perovskites have attracted much interest for the development of next-generation optoelectronic devices due to their outstanding figures of merit in photovoltaics, exceeding 23% power conversion efficiency (PCE),¹ and in light emitting devices (LEDs), with nearly 100% internal quantum efficiency,² together with defect tolerance, low-cost solution processing and tunable emission across the visible spectrum.³⁻⁵ However, these devices suffer from severe limitations, such as low ambient stability,⁴ ion migration under operation,^{4,6} and the presence of toxic Pb.⁴ In this respect, the substitution of Pb²⁺ by the combination of trivalent (Bi³⁺, Sb³⁺) and monovalent (Ag⁺, Cu⁺, Au⁺, K⁺) cations leads to the formation of double perovskites, which demonstrated ambient stability, but inferior device performance compared to Pb-halide perovskites.^{4,7,8} The Cs₂AgBiBr₆ double perovskite has demonstrated good performance in solar cells reaching a PCE 2.84%,⁹⁻¹⁵ and in photodetectors with a high detectivity of 3.29×10^{12} Jones and fast response of 17 ns,¹⁶ as well as application in X-Ray detectors¹⁷ and memristors.¹⁸ The optoelectronic properties of Cs₂AgBiBr₆ stimulated the development of low-dimensional (2D) perovskites from their 3D counterparts by the introduction of large A-site cations. These layered double perovskites feature many interesting properties, for example the transition from an indirect to a direct band gap material by tuning the number of adjacent octahedra layers.¹⁹⁻²² However, for their further development, it is essential to understand how the crystal structure and lattice dynamics affect the optical and electronic properties, and their relation to electron-phonon coupling and phase transitions.²³⁻²⁵

In this work, we study layered double perovskites derived from Cs₂AgBiBr₆ focusing on the influence of the organic cation layer on the optical and vibrational properties. We use a series of alkyl and phenyl ammonium cations with varying size and structure, and grow crystals with single (1L) and double (2L) octahedra layers. Temperature-dependent micro-Raman spectroscopy allows

to determine the presence or absence of phase transitions. We show that the intermolecular interactions between the ammonium alkyl-chain cations and the inorganic octahedral layer are closely related to phase transitions in the 1L layered crystal structures. Concerning the emission properties, the photoluminescence (PL) spectra strongly depend on the number of adjacent octahedral layers in the crystal structure as well as on a structural phase transition. This is in agreement with the transition from an indirect band gap for the 3D crystal^{21,23,25–28} to a direct band gap for the 1L system¹⁹. The influence of the octahedral distortions on the optical properties may be enhanced by an extremely flat conduction band (CB) in 1L compounds, such that minor structural changes are sufficient to affect them. Our work provides novel insights into the correlation of structural and optical properties in layered double perovskites, and demonstrates how the proper selection of the organic cations can be used to avoid or deliberately trigger phase transitions, with application in devices for improved thermal stability,¹⁴ or exploiting switching.²⁹

We synthesized layered double perovskite crystals derived from the $\text{Cs}_2\text{AgBiBr}_6$ (3D) system using revised recipes^{19,30}. To evaluate the effect of length and stereochemistry of the organic moieties on the interaction between octahedra layers, we selected a series of alkyl cations and a phenyl cation, concretely: propylammonium (PA), butylammonium (BA), phenylethylammonium (PEA), decylammonium (DA) and dodecylammonium (DoA) (see Figure 1a-g and Supporting Information (SI), Experimental methods section and Figure S1). By selecting the concentrations of the organic moieties and inorganic precursors (BiBr_3 , AgBr and CsBr), we obtained $(\text{R-NH}_3^+)_4\text{AgBiBr}_8$ crystals that consists of single octahedra layers separated by organic cations (hereafter referred to as 1L), and $(\text{R-NH}_3^+)_2\text{CsAgBiBr}_7$ crystals with two adjacent octahedra layers enabled by the presence of Cs^+ (noted as 2L) (see Figure 1d-f).¹⁹ X-ray diffraction (XRD) spectra of the different samples are shown in Figure S2 and allow for the 1L systems to directly evaluate

the inter-distance between the octahedra layers (d) (Figure 1h). Here, the d value increases with the length of the molecules up to 20–23 Å, after which the alkyl chains start to cross or entangle as depicted in Figure S3, in agreement with literature^{19,20}.

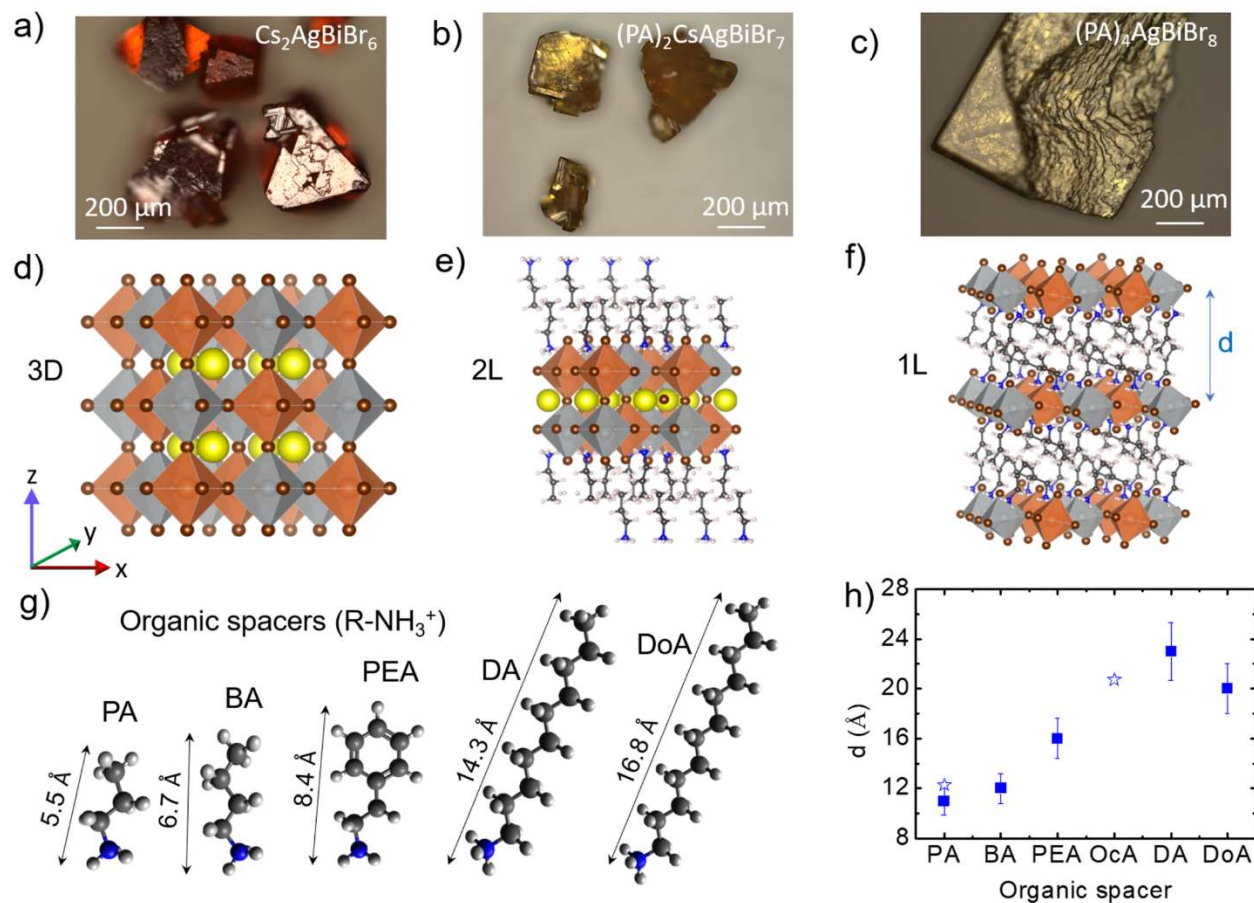


Figure 1. (a-c) Representative optical microscope images of the 3D $\text{Cs}_2\text{AgBiBr}_6$ crystals, and $(\text{PA})_2\text{CsAgBiBr}_7$ (2L) and $(\text{PA})_4\text{AgBiBr}_8$ (1L) layered perovskites. (d-f) Crystal structures of the 3D, 2L-PA and 1L-PA samples, drawn using VESTA 3 software³¹ based on the crystallographic data from refs^{19,20}. In (c) the octahedra layers inter-distance is indicated as d . (g) Schemes of the ammonium cations used in this work and their length estimated using Avogadro software.³² (h) Inter-distance between the octahedra layers (d) for the 1L samples with the different organic

moieties obtained from XRD analysis. Additionally, values from literature²⁰ are displayed with stars for PA and octylammonium (OcA) perovskites.

The Raman spectra of the 3D, PA, BA, PEA and DA systems recorded at 80K are shown in Figure 2a in the 100-300 cm^{-1} spectral range. All spectra show a dominant peak in the range around 170 cm^{-1} that is assigned to the A_{1g} mode³³ related to stretching of the $(\text{AgBr}_6)^{5-}$ and $(\text{BiBr}_6)^{3-}$ octahedra.^{23,34} The A_{1g} is also associated to the longitudinal-optical (LO) phonon of the inorganic lattice,³⁴⁻³⁶ and occurs at the highest frequency (178 cm^{-1}) for the 3D crystal, due to its higher stiffness compared to the 2L and 1L crystals (in this order), which is reasonable due to the fully inorganic structure in all three spatial dimensions. Indeed, compared to the 3D crystal, the introduction of the organic layers leads to a red shift of the A_{1g} mode (Figure 2b), which is clearly more pronounced for the 1L samples, in which the organic layers are in contact with all octahedra (such behavior is also observed at room temperature, see Figure S5a-b). Interestingly, the A_{1g} mode for the PEA system does not follow this trend, since here the red shift is significant already for the 2L structure. This difference could be attributed to the different stereochemistry and arrangement of the phenyl rings, compared to the alkyl ammonium moieties, that result in a $\pi - \pi$ stacking in the organic layer.^{37,38} The deviation of A_{1g} mode in 1L-DA sample is possibly due to alkyl chains entanglement causing higher stiffness than in the other 1L-crystals. Furthermore, distortions and octahedral tilts in the inorganic layer can affect the phonon modes, as will be discussed later on. For the layered systems a second, much weaker, peak can be identified around 140 cm^{-1} that we assign to a vibrational mode with E_g symmetry.^{23,34} Additionally we do not observe differences in the Raman spectrum when the material is mechanically exfoliated in form of flakes compared to the bulk crystal (Figure S5c).

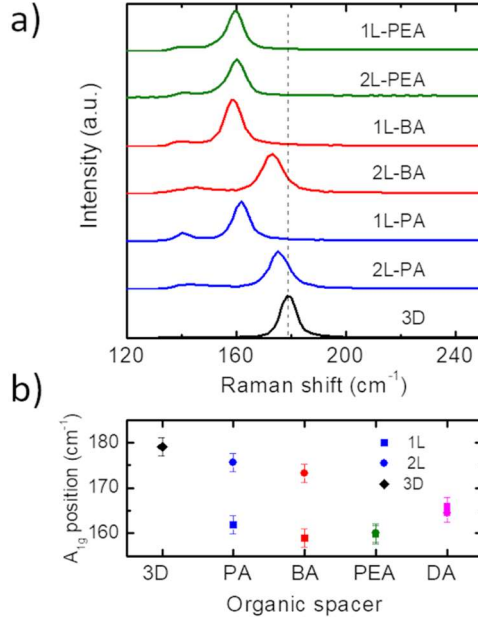


Figure 2. (a) Raman spectra recorded with a micro-setup in the spectral range of the A_{1g} mode from the 3D crystal and layered systems with PA, BA and PEA organic moieties. Temperature was 80K, and the laser excitation wavelength was 532 nm. (b) Spectral position of the A_{1g} mode for the different samples.

Temperature-dependent Raman data for the 3D, BA, PA, and PEA systems are shown in Figure 3 (see Figure S6-S9 for additional data). For the 3D crystal, a careful inspection of the A_{1g} Raman band reveals a slight change of the mode frequency (~ 2 cm⁻¹ at 125-150K, accompanied by a peak broadening, Figure S6). This behavior can be ascribed to a phase transition from tetragonal to cubic structure,²⁵ also observed for other double perovskites.³⁹ Noteworthy, for the 1L systems the temperature-dependent behavior is strongly influenced by the type of the organic moiety, and shows abrupt shifts at well-defined temperatures (indicated by the white dashed lines) for the 1L-PA (~ 172 K) and 1L-BA (~ 282 K) samples. For both samples we observe a blue shift of the A_{1g} mode, accompanied by a sudden broadening, with increasing temperature in this region. Comparison of the A_{1g} Raman band with the vibrational bands of the molecules in the 1100-1700

cm⁻¹ range around the transition temperature reveals a concomitant abrupt broadening of the CH₂ and NH₃ vibrational bands^{40,41} (Figure S10-S11). This correlation demonstrates a stringent relation of the conformational arrangement of the molecules in the organic layer to the vibrational modes of the inorganic octahedra. These primary amines are known to undergo a transition from the solid to the liquid phase at 200K for PA and at 224K for BA.⁴² This is in good agreement with our observation that the phase-transition occurs at higher temperatures in 1L-BA than in 1L-PA. We can therefore conclude that the transition in the organic layer triggers a structural change in the octahedra layer that we assign to modifications in the octahedral tilt pattern, as reported in ref.¹⁹. Illustrations of such different tilt patterns are depicted in Figure S4. Furthermore, we note that the arrangement of the disordered phase in the organic layer, which correlates with a marked tilting of the octahedra, results in a blue shift of the A_{1g} mode compared to the ordered phase, where there is a less distorted octahedra lattice. Similarly, the red shift of the A_{1g} mode in the low-dimensional systems (with respect to the frequency of the 3D system – see Figure 2) reflects how the organic layer acts on the inorganic octahedra lattice.

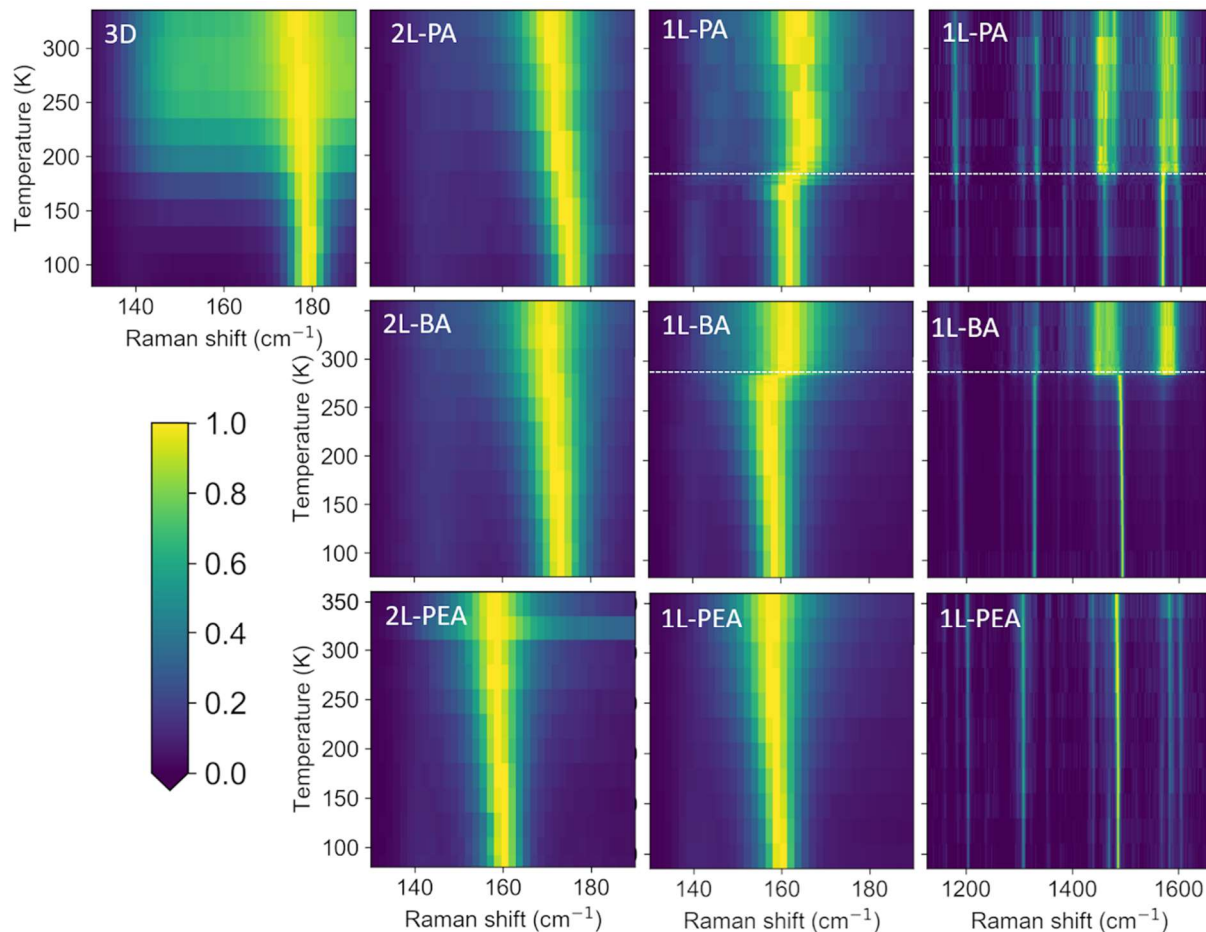


Figure 3. Temperature-dependent Raman spectra in the range of the A_{1g} band for the PA, BA and PEA systems and the 3D crystal. For the 1L systems also spectra in the range from 1100-1700 cm^{-1} are shown, in which the vibrational resonances of the organic cations occur. The horizontal dashed lines indicate the temperature in which the A_{1g} mode in the 1L-PA and 1L-BA samples undergoes a sudden shift, coinciding with a drastic change in the width of the molecular vibrational modes around 1200 cm^{-1} (C-N stretching), 1340 cm^{-1} (CH_2 twisting/wagging type), 1500 cm^{-1} (CH_2 bending) and 1600 cm^{-1} (NH_3^+ bending).^{40,41} For the PEA system, no shift of the A_{1g} mode or linewidth broadening of the Raman modes related to molecular vibrations are observed.

The distortion of the octahedra lattice significantly affects the electronic structure and the transition from an indirect to a direct band gap, and therefore is of paramount importance for the optical properties. We quantify the lattice distortion from the corresponding crystallographic data by the parameter λ_{Ag-Br} that expresses the deviation of the Ag-Br bond length compared to the undistorted Ag-Br octahedra lattice (see details in the SI and Table S3). This parameter λ_{Ag-Br} increases from 3D to 2L and from 2L to 1L, and depends on the type of the organic moiety.

To relate the distortions and the vibrational modes to the optical properties and the electronic band structure, we performed temperature-dependent absorbance and PL measurements, and band structure calculations using density-functional theory (DFT) for different systems. In the absorbance spectra recorded from 3D, 2L-PA, and 1L-PA samples at different temperatures (Figure 4a, and Figure S12-S14 and Table S4 for additional data), we do not find any significant shift of the absorption peak related to the direct bandgap,²⁷ but only a slight broadening with increasing temperature, in agreement with literature.¹⁹ However, the crystal structure of the samples has a strong impact on the position of the absorption peak that blue-shifts when passing from 3D to 2L to 1L (Figure S13).

Concerning the PL properties shown in Figure 4b (see Figures S15-16 for additional data), for the 3D sample at 80K, we observe a broad emission peak centered ~ 2 eV, and similarly for the 2L samples, as reported in literature^{19,27,28}. Although this emission was firstly related to color centers,^{21,23,25} recent reports support an indirect exciton recombination, which could be accompanied by a weak blue PL emission close to the absorption peak position,^{27,28,43} and in agreement with the strong electron-phonon coupling found in these materials^{23,34} (see Table S5). For the 1L samples, a broad and asymmetric peak with a maximum at ~ 3 eV is observed, similar

to what has been reported for 1L-BA at 80K,¹⁹ and ascribed to fast recombination at the direct band edge.^{19,27,28}

Regarding the temperature dependence (Figure 4c), the PL intensity of the 3D, 2L-PA and 1L-PA samples strongly increases below the corresponding phase transition temperatures (122K,²⁵ 222K⁴⁴ and 172K, respectively). However, the change in the PL intensity around the phase transition is more marked in the case of the 1L-PA, with an increase of $\sim 95\%$ in 15K, while below the transition temperature is relatively stable with only a minor decrease ($\sim 12\%$ in 42K). This could be attributed to the conformational changes of the organic moieties detected by Raman spectroscopy (Figure 3), which can affect the band structure as extracted from our DFT calculations discussed below.

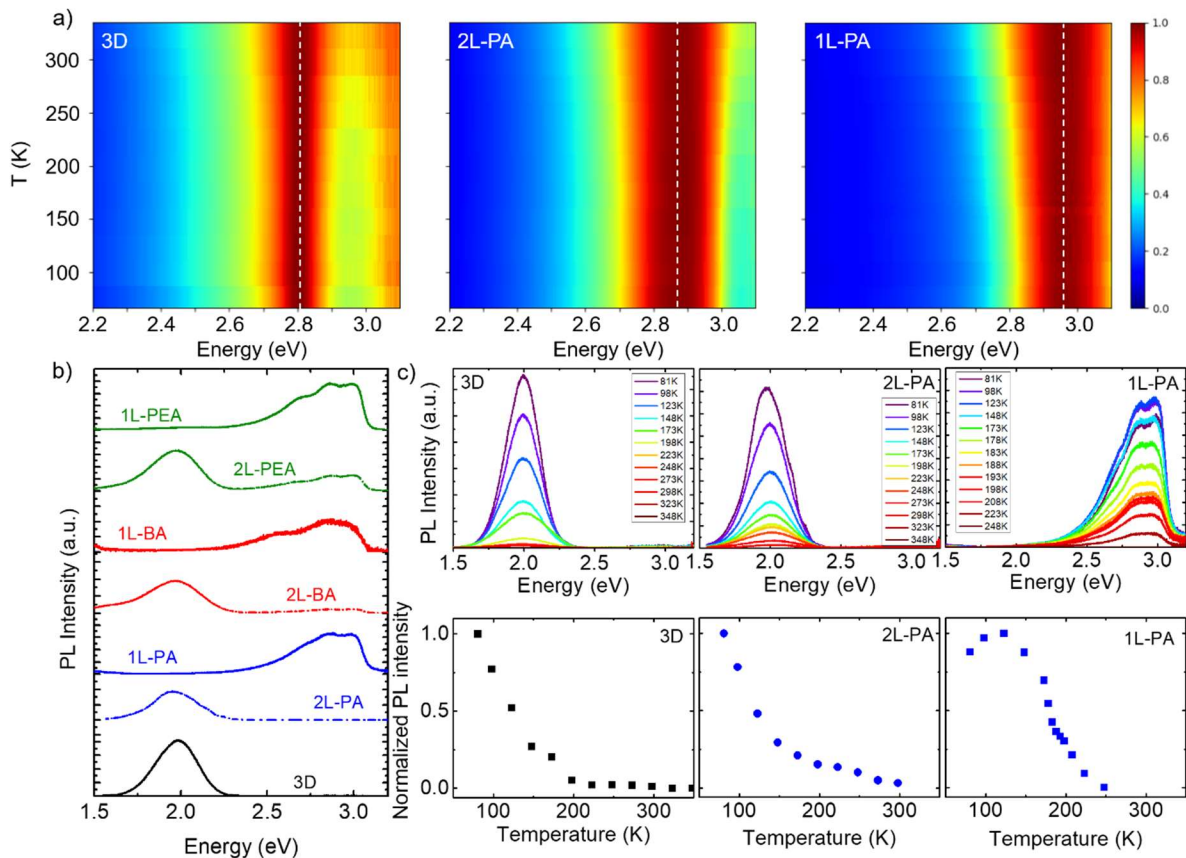


Figure 4. (a) Normalized spectral intensity maps of the temperature-dependent absorbance for 3D, 2L and 1L PA-films. The dashed line indicates the position of the absorption peak. (b) Photoluminescence spectra of the 3D, and the PA, BA, and PEA systems recorded from the corresponding crystals at 80K and laser excitation wavelength at 325 nm. (c) Temperature-dependent PL spectra of the 3D, 2L-PA and 1L-crystals (top), and the evolution of the PL intensity (bottom).

To gain deeper understanding of the influence of the phase transition on the optical properties, we calculate the band structure^{45,46} for the 1L-BA and 2L-BA crystals above and below the transition temperature, including 1L-PA and 2L-PA structures at room temperature to evaluate the effect of the organic cation. Our calculations revealed a strong influence of spin-orbit coupling (Figure S17), inducing a splitting of 1 eV of the lowest CB. The analysis of low- and room-temperature band structures was performed for 1L-BA and 2L-BA systems (Figure 5a-c). Similar behaviors can be expected at low-temperatures for the 1L-PA and 1L-BA systems, since the band structures of 1L-PA and 1L-BA at room-temperature (Figure 5c,d) are almost identical within a 5 eV energy window around the Fermi level. This is in line with the absence of organic states close to the Fermi level, the only difference in the two compounds being an extra CH₂ group on the alkyl chain. Both 1L-PA and 1L-BA are likely to have similar distortions of the inorganic framework, which is corroborated by additional calculations on the 2L-BA and 2L-PA structures (Figure S18).

The calculated bands and density of states of 1L structures are in agreement with those reported in literature¹⁹, showing a direct band gap at the Γ point with Br-4*p* and Ag-4*d* orbitals forming the top valence band and Bi-6*p* and Br-4*p* orbitals forming the CBs. Consistently with Ref.¹⁹, an indirect band gap is obtained for the 2L-system (Figure 5b and Figure S18).

The 1L-BA structure features different octahedral tilt patterns at low- and room-temperatures. At 298K the octahedral tilts are within xz plane ($a^0b^+c^0$ in Glazer's notation⁴⁷), while below the transition temperature a tilt in the xy plane appears ($a^0a^0c^-$). A striking feature of 1L structures is a rather flat bottom CB, which is related to the strong decrease of Bi-Bi hopping integral due to energetically well-separated Ag orbitals within the checkerboard ordering of the metal ions (Figure S19a). Indeed, in 2L structures with shorter Ag-Br bonds along the c axis and higher number of connected octahedra than the 1L systems, the dispersion of the lowest CB is much larger (~ 0.5 eV). The increased amplitude of the $a^0b^+c^0$ octahedral tilt at room temperature causes the splitting of 0.1 eV of the lowest conduction and the highest valence bands. Combined with the flatness of the bands, this makes possible for small distortions to produce significant changes in the band structure across the bandgap, thus affecting the optical properties. This could be at the origin of the change in PL intensity observed around the phase transition temperature for the 1L-PA sample. Since the CB is essentially flat, the transition energy remains almost unchanged, in good agreement with our absorption and PL results. Additionally, thermally excited polar modes could cause a shift in the CB minimum *via* the Rashba effect, leading to indirect bandgap (discussion in Figure S19b). However, these modes are not visible in the centrosymmetric 1L crystal structures experimentally determined^{19,21}.

Overall, the analysis of the band structures of 1L-BA system above and below the phase transition temperature shows how variations in octahedral tilt patterns mostly affect the flat CB, opening interesting perspectives on the effects of electron-phonon coupling on these materials.

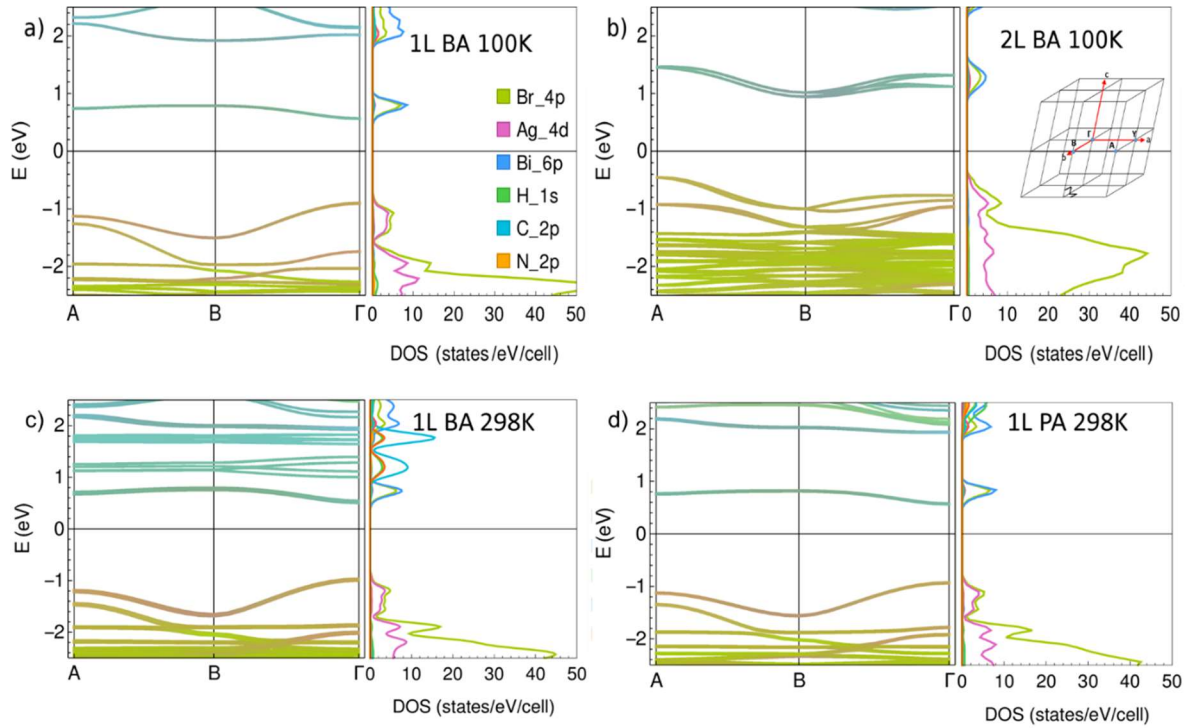


Figure 5. Band structure and projected density of states of (a) 1L-BA at 100K, (b) 2L-BA at 100K, (c) 1L-BA at 298K and (d) 1L-PA at 298K. The colors encode the contribution of corresponding atomic orbitals to the states at each k -point. Inset: (b) the Brillouin zone and high-symmetry points used in the band structure plots.

In summary, we performed a systematic study of layered crystals derived from the $\text{Cs}_2\text{AgBiBr}_6$ double perovskite, consisting of single layers (1L) or bilayers (2L) of inorganic octahedra with organic moieties of different length and structure. Our work elucidates the interplay of lattice vibrations, crystal phases and optical properties combining temperature-dependent Raman, absorbance, and photoluminescence spectroscopy with DFT modeling. Here we show that changes in the conformational rearrangement, from a “*solid-like*” phase (ordered) to “*liquid-like*” (disordered) one, of the organic cations can translate to phase transitions in the layered crystals,

and that such transitions influence the PL intensity, but not the emission wavelength. Our findings open pathways to manipulate this organic-mediated phase transition by properly selecting the ammonium moieties. The possibility to independently tune the band gap (*via* the composition of the octahedral layers) and structural phase transitions (*via* the choice of organic moieties) in these materials is appealing towards applications in optoelectronic devices such as solar cells or LEDs in terms of thermal stability. In addition, these properties can be exploited in devices using the phase transition for active switching.

ASSOCIATED CONTENT

Supporting Information. Experimental methods; Optical microscope images; XRD patterns and analysis; Raman spectra at room temperature; detailed Raman spectroscopy characterization; additional absorbance and PL spectroscopy characterization; and Computational details.

AUTHOR INFORMATION

Corresponding Author

*Beatriz Martín-García (b.martingarcia@nanogune.eu) and Davide Spirito (spirito@ihp-microelectronics.com)

Notes

The manuscript was written through contributions of all authors. All authors have given approval to the final version of the manuscript. ‡The authors B.M-G. and D.S. contributed equally. G.B. and S.A. performed the DFT modelling. The authors declare no competing financial interest.

ACKNOWLEDGMENT

B.M-G. and F.B. acknowledge the funding from the European Union's Horizon 2020 research and innovation programme under grant agreement no. 785219 (GrapheneCore2). B.M-G. thanks also to Gipuzkoa Council (Spain) in the frame of Gipuzkoa Fellows Program. D.S. acknowledges the funding from the German Research Foundation (DFG) within the project ESSENCE. This work is supported by the Spanish MINECO under the María de Maeztu Units of Excellence Programme (MDM-2016-0618). We thank Prof. G. Capellini (IHP) for fruitful discussions regarding the experimental spectroscopic set-up and Dr. D. Kot (IHP) for the assistance with the temperature-dependent absorbance set-up. We acknowledge Dr. M. Prato for the access to the Materials Characterization Facility – IIT for the XRD characterization, and Dr. A. Toma for the access and E. Rondanina for her assistance in the laser-writer patterning of markers on Si/SiO₂ substrates at the Clean Room Facility – IIT.

REFERENCES

- (1) NREL. Best Research-Cell Efficiency Chart <https://www.nrel.gov/pv/cell-efficiency.html> (accessed Mar 25, 2020).
- (2) Zhao, B.; Bai, S.; Kim, V.; Lamboll, R.; Shivanna, R.; Auras, F.; Richter, J. M.; Yang, L.; Dai, L.; Alsari, M.; et al. High-Efficiency Perovskite–Polymer Bulk Heterostructure Light-Emitting Diodes. *Nat. Photonics* **2018**, *12* (12), 783–789. <https://doi.org/10.1038/s41566-018-0283-4>.
- (3) Grancini, G.; Nazeeruddin, M. K. Dimensional Tailoring of Hybrid Perovskites for Photovoltaics. *Nat. Rev. Mater.* **2019**, *4* (1), 4–22. <https://doi.org/10.1038/s41578-018-0065-0>.
- (4) Jena, A. K.; Kulkarni, A.; Miyasaka, T. Halide Perovskite Photovoltaics: Background, Status, and Future Prospects. *Chem. Rev.* **2019**, *119* (5), 3036–3103. <https://doi.org/10.1021/acs.chemrev.8b00539>.
- (5) Smith, M. D.; Connor, B. A.; Karunadasa, H. I. Tuning the Luminescence of Layered Halide Perovskites. *Chem. Rev.* **2019**, *119* (5), 3104–3139. <https://doi.org/10.1021/acs.chemrev.8b00477>.
- (6) Capasso, A.; Matteocci, F.; Najafi, L.; Prato, M.; Buha, J.; Cinà, L.; Pellegrini, V.; Carlo, A. D.; Bonaccorso, F. Few-Layer MoS₂ Flakes as Active Buffer Layer for Stable Perovskite Solar Cells. *Adv Energy Mater* **2016**, *6* (16), 1600920. <https://doi.org/10.1002/aenm.201600920>.
- (7) Xiao, Z.; Song, Z.; Yan, Y. From Lead Halide Perovskites to Lead-Free Metal Halide Perovskites and Perovskite Derivatives. *Adv. Mater.* **2019**, 1803792. <https://doi.org/10.1002/adma.201803792>.

- (8) Vargas, B.; Rodríguez-López, G.; Solis-Ibarra, D. The Emergence of Halide Layered Double Perovskites. *ACS Energy Lett.* **2020**, *5* (11), 3591–3608. <https://doi.org/10.1021/acsenergylett.0c01867>.
- (9) Greul, E.; Petrus, M. L.; Binek, A.; Docampo, P.; Bein, T. Highly Stable, Phase Pure Cs₂AgBiBr₆ Double Perovskite Thin Films for Optoelectronic Applications. *J. Mater. Chem. A* **2017**, *5* (37), 19972–19981. <https://doi.org/10.1039/C7TA06816F>.
- (10) Wang, M.; Zeng, P.; Bai, S.; Gu, J.; Li, F.; Yang, Z.; Liu, M. High-Quality Sequential-Vapor-Deposited Cs₂AgBiBr₆ Thin Films for Lead-Free Perovskite Solar Cells. *Sol. RRL* **2018**, *2* (12), 1800217. <https://doi.org/10.1002/solr.201800217>.
- (11) Pantaler, M.; Cho, K. T.; Queloz, V. I. E.; García Benito, I.; Fettiukhauer, C.; Anusca, I.; Nazeeruddin, M. K.; Lupascu, D. C.; Grancini, G. Hysteresis-Free Lead-Free Double-Perovskite Solar Cells by Interface Engineering. *ACS Energy Lett.* **2018**, *3* (8), 1781–1786. <https://doi.org/10.1021/acsenergylett.8b00871>.
- (12) Igbari, F.; Wang, R.; Wang, Z.-K.; Ma, X.-J.; Wang, Q.; Wang, K.-L.; Zhang, Y.; Liao, L.-S.; Yang, Y. Composition Stoichiometry of Cs₂AgBiBr₆ Films for Highly Efficient Lead-Free Perovskite Solar Cells. *Nano Lett.* **2019**, *19* (3), 2066–2073. <https://doi.org/10.1021/acs.nanolett.9b00238>.
- (13) Zhang, Z.; Wu, C.; Wang, D.; Liu, G.; Zhang, Q.; Luo, W.; Qi, X.; Guo, X.; Zhang, Y.; Lao, Y.; et al. Improvement of Cs₂AgBiBr₆ Double Perovskite Solar Cell by Rubidium Doping. *Org. Electron.* **2019**, *74*, 204–210. <https://doi.org/10.1016/j.orgel.2019.06.037>.
- (14) Wu, C.; Zhang, Q.; Liu, Y.; Luo, W.; Guo, X.; Huang, Z.; Ting, H.; Sun, W.; Zhong, X.; Wei, S.; et al. The Dawn of Lead-Free Perovskite Solar Cell: Highly Stable Double Perovskite Cs₂AgBiBr₆ Film. *Adv. Sci.* **2018**, *5* (3), 1700759. <https://doi.org/10.1002/advs.201700759>.
- (15) Yang, X.; Wang, W.; Ran, R.; Zhou, W.; Shao, Z. Recent Advances in Cs₂AgBiBr₆-Based Halide Double Perovskites as Lead-Free and Inorganic Light Absorbers for Perovskite Solar Cells. *Energy Fuels* **2020**, *34* (9), 10513–10528. <https://doi.org/10.1021/acs.energyfuels.0c02236>.
- (16) Yang, J.; Bao, C.; Ning, W.; Wu, B.; Ji, F.; Yan, Z.; Tao, Y.; Liu, J.; Sum, T. C.; Bai, S.; et al. Stable, High-Sensitivity and Fast-Response Photodetectors Based on Lead-Free Cs₂AgBiBr₆ Double Perovskite Films. *Adv. Opt. Mater.* **2019**, 1801732. <https://doi.org/10.1002/adom.201801732>.
- (17) Pan, W.; Wu, H.; Luo, J.; Deng, Z.; Ge, C.; Chen, C.; Jiang, X.; Yin, W.-J.; Niu, G.; Zhu, L.; et al. Cs₂AgBiBr₆ Single-Crystal X-Ray Detectors with a Low Detection Limit. *Nat. Photonics* **2017**, *11* (11), 726–732. <https://doi.org/10.1038/s41566-017-0012-4>.
- (18) Cheng, X.; Qian, W.; Wang, J.; Yu, C.; He, J.; Li, H.; Xu, Q.; Chen, D.; Li, N.; Lu, J. Environmentally Robust Memristor Enabled by Lead-Free Double Perovskite for High-Performance Information Storage. *Small* **2019**, *15* (49), 1905731. <https://doi.org/10.1002/sml.201905731>.
- (19) Connor, B. A.; Leppert, L.; Smith, M. D.; Neaton, J. B.; Karunadasa, H. I. Layered Halide Double Perovskites: Dimensional Reduction of Cs₂AgBiBr₆. *J. Am. Chem. Soc.* **2018**, *140* (15), 5235–5240. <https://doi.org/10.1021/jacs.8b01543>.
- (20) Mao, L.; Teicher, S. M. L.; Stoumpos, C. C.; Kennard, R. M.; DeCrescent, R. A.; Wu, G.; Schuller, J. A.; Chabinye, M. L.; Cheetham, A. K.; Seshadri, R. Chemical and Structural Diversity of Hybrid Layered Double Perovskite Halides. *J. Am. Chem. Soc.* **2019**, *141* (48), 19099–19109. <https://doi.org/10.1021/jacs.9b09945>.

- (21) Fang, Y.; Zhang, L.; Wu, L.; Yan, J.; Lin, Y.; Wang, K.; Mao, W. L.; Zou, B. Pressure-Induced Emission (PIE) and Phase Transition of a Two-dimensional Halide Double Perovskite (BA)₄AgBiBr₈ (BA=CH₃(CH₂)₃NH₃⁺). *Angew. Chem. Int. Ed.* **2019**, *58* (43), 15249–15253. <https://doi.org/10.1002/anie.201906311>.
- (22) McClure, E. T.; McCormick, A. P.; Woodward, P. M. Four Lead-Free Layered Double Perovskites with the *n* = 1 Ruddlesden–Popper Structure. *Inorg. Chem.* **2020**, *59* (9), 6010–6017. <https://doi.org/10.1021/acs.inorgchem.0c00009>.
- (23) Zelewski, S. J.; Urban, J. M.; Surrente, A.; Maude, D. K.; Kuc, A.; Schade, L.; Johnson, R. D.; Dollmann, M.; Nayak, P. K.; Snaith, H. J.; et al. Revealing the Nature of Photoluminescence Emission in the Metal-Halide Double Perovskite Cs₂AgBiBr₆. *J. Mater. Chem. C* **2019**, *7* (27), 8350–8356. <https://doi.org/10.1039/C9TC02402F>.
- (24) Kentsch, R.; Scholz, M.; Horn, J.; Schlettwein, D.; Oum, K.; Lenzer, T. Exciton Dynamics and Electron–Phonon Coupling Affect the Photovoltaic Performance of the Cs₂AgBiBr₆ Double Perovskite. *J. Phys. Chem. C* **2018**, *122* (45), 25940–25947. <https://doi.org/10.1021/acs.jpcc.8b09911>.
- (25) Schade, L.; Wright, A. D.; Johnson, R. D.; Dollmann, M.; Wenger, B.; Nayak, P. K.; Prabhakaran, D.; Herz, L. M.; Nicholas, R.; Snaith, H. J.; et al. Structural and Optical Properties of Cs₂AgBiBr₆ Double Perovskite. *ACS Energy Lett.* **2019**, *4* (1), 299–305. <https://doi.org/10.1021/acsenergylett.8b02090>.
- (26) Su, J.; Mou, T.; Wen, J.; Wang, B. First-Principles Study on the Structure, Electronic, and Optical Properties of Cs₂AgBiBr_{6-x}Cl_x Mixed-Halide Double Perovskites. *J. Phys. Chem. C* **2020**, *124* (9), 5371–5377. <https://doi.org/10.1021/acs.jpcc.9b11827>.
- (27) Schmitz, A.; Schaberg, L. L.; Sirotinskaya, S.; Pantaler, M.; Lupascu, D. C.; Benson, N.; Bacher, G. Fine Structure of the Optical Absorption Resonance in Cs₂AgBiBr₆ Double Perovskite Thin Films. *ACS Energy Lett.* **2020**, *5* (2), 559–565. <https://doi.org/10.1021/acsenergylett.9b02781>.
- (28) Dey, A.; Richter, A. F.; Debnath, T.; Huang, H.; Polavarapu, L.; Feldmann, J. Transfer of Direct to Indirect Bound Excitons by Electron Intervalley Scattering in Cs₂AgBiBr₆ Double Perovskite Nanocrystals. *ACS Nano* **2020**, *14* (5), 5855–5861. <https://doi.org/10.1021/acsnano.0c00997>.
- (29) Zeb, A.; Sun, Z.; Khan, A.; Zhang, S.; Khan, T.; Asghar, M. A.; Luo, J. [C₆H₁₄N]PbI₃: A One-Dimensional Perovskite-like Order–Disorder Phase Transition Material with Semiconducting and Switchable Dielectric Attributes. *Inorg. Chem. Front.* **2018**, *5* (4), 897–902. <https://doi.org/10.1039/C7QI00722A>.
- (30) Slavney, A. H.; Hu, T.; Lindenberg, A. M.; Karunadasa, H. I. A Bismuth-Halide Double Perovskite with Long Carrier Recombination Lifetime for Photovoltaic Applications. *J. Am. Chem. Soc.* **2016**, *138* (7), 2138–2141. <https://doi.org/10.1021/jacs.5b13294>.
- (31) Momma, K.; Izumi, F. VESTA 3 for Three-Dimensional Visualization of Crystal, Volumetric and Morphology Data. *J. Appl. Crystallogr.* **2011**, *44* (6), 1272–1276. <https://doi.org/10.1107/S0021889811038970>.
- (32) Hanwell, M. D.; Curtis, D. E.; Lonie, D. C.; Vandermeersch, T.; Zurek, E.; Hutchison, G. R. Avogadro: An Advanced Semantic Chemical Editor, Visualization, and Analysis Platform. *J. Cheminformatics* **2012**, *4* (1), 17. <https://doi.org/10.1186/1758-2946-4-17>.
- (33) To make the assignment easier to follow, we kept the notation A_{1g} throughout the text. However, the A_{1g} mode is from the representation of O_h, that refers to the point group of 3D crystal. The derived layered crystals from 3D have a point group C_{2h}, and therefore, the A_{1g}

- mode in O_h corresponds to the A_g mode in C_{2h} . In the same way, the E_g mode for O_h in 3D splits in two A_g modes in C_{2h} .
- (34) Steele, J. A.; Puech, P.; Keshavarz, M.; Yang, R.; Banerjee, S.; Debroye, E.; Kim, C. W.; Yuan, H.; Heo, N. H.; Vanacken, J.; et al. Giant Electron–Phonon Coupling and Deep Conduction Band Resonance in Metal Halide Double Perovskite. *ACS Nano* **2018**, *12* (8), 8081–8090. <https://doi.org/10.1021/acsnano.8b02936>.
 - (35) Dahod, N. S.; France-Lanord, A.; Paritmongkol, W.; Grossman, J. C.; Tisdale, W. A. Low-Frequency Raman Spectrum of 2D Layered Perovskites: Local Atomistic Motion or Superlattice Modes? *J. Chem. Phys.* **2020**, *153* (4), 044710. <https://doi.org/10.1063/5.0012763>.
 - (36) Mauck, C. M.; France-Lanord, A.; Hernandez Oendra, A. C.; Dahod, N. S.; Grossman, J. C.; Tisdale, W. A. Inorganic Cage Motion Dominates Excited-State Dynamics in 2D-Layered Perovskites $(C_xH_{2x+1}NH_3)_2PbI_4$ ($x = 4–9$). *J. Phys. Chem. C* **2019**, *123* (45), 27904–27916. <https://doi.org/10.1021/acs.jpcc.9b07933>.
 - (37) Dhanabalan, B.; Leng, Y.-C.; Biffi, G.; Lin, M.-L.; Tan, P.-H.; Infante, I.; Manna, L.; Arciniegas, M. P.; Krahn, R. Directional Anisotropy of the Vibrational Modes in 2D-Layered Perovskites. *ACS Nano* **2020**, *14* (4), 4689–4697. <https://doi.org/10.1021/acsnano.0c00435>.
 - (38) Gong, X.; Voznyy, O.; Jain, A.; Liu, W.; Sabatini, R.; Piontkowski, Z.; Walters, G.; Bappi, G.; Nokhrin, S.; Bushuyev, O.; et al. Electron–Phonon Interaction in Efficient Perovskite Blue Emitters. *Nat. Mater.* **2018**, *17* (6), 550–556. <https://doi.org/10.1038/s41563-018-0081-x>.
 - (39) Krylov, A. S.; Vtyurin, A. N.; Bulou, A.; Voronov, V. N. Raman Spectra and Phase Transitions in the Rb_2KScF_6 Elpasolite. *Ferroelectrics* **2003**, *284* (1), 47–64. <https://doi.org/10.1080/00150190390204709>.
 - (40) da Costa, A. M. A.; Geraldés, C. F. G. C.; Teixeira-Dias, J. J. C. A Raman Spectroscopic Study of Molecular Interaction in Long-Chain Primary Amines Systems. *J. Raman Spectrosc.* **1982**, *13* (1), 56–62. <https://doi.org/10.1002/jrs.1250130111>.
 - (41) Abid, H.; Trigui, A.; Mlayah, A.; Hlil, E. K.; Abid, Y. Phase Transition in Organic–Inorganic Perovskite $(C_9H_{19}NH_3)_2PbI_2Br_2$ of Long-Chain Alkylammonium. *Results Phys.* **2012**, *2*, 71–76. <https://doi.org/10.1016/j.rinp.2012.04.003>.
 - (42) Maloney, A. G. P.; Wood, P. A.; Parsons, S. Competition between Hydrogen Bonding and Dispersion Interactions in the Crystal Structures of the Primary Amines. *CrystEngComm* **2014**, *16* (19), 3867–3882. <https://doi.org/10.1039/C3CE42639D>.
 - (43) Palummo, M.; Berrios, E.; Varsano, D.; Giorgi, G. Optical Properties of Lead-Free Double Perovskites by Ab Initio Excited-State Methods. *ACS Energy Lett.* **2020**, *5* (2), 457–463. <https://doi.org/10.1021/acsenergylett.9b02593>.
 - (44) Zhang, W.; Hong, M.; Luo, J. Halide Double Perovskite Ferroelectrics. *Angew. Chem. Int. Ed.* **2020**, *59* (24), 9305–9308. <https://doi.org/10.1002/anie.201916254>.
 - (45) Soler, J. M.; Artacho, E.; Gale, J. D.; García, A.; Junquera, J.; Ordejón, P.; Sánchez-Portal, D. The SIESTA Method for Ab Initio Order- N Materials Simulation. *J. Phys. Condens. Matter* **2002**, *14* (11), 2745–2779. <https://doi.org/10.1088/0953-8984/14/11/302>.
 - (46) Giannozzi, P.; Baroni, S.; Bonini, N.; Calandra, M.; Car, R.; Cavazzoni, C.; Ceresoli, D.; Chiarotti, G. L.; Cococcioni, M.; Dabo, I.; et al. QUANTUM ESPRESSO: A Modular and Open-Source Software Project for Quantum Simulations of Materials. *J. Phys. Condens. Matter* **2009**, *21* (39), 395502. <https://doi.org/10.1088/0953-8984/21/39/395502>.

- (47) Glazer, A. M. The Classification of Tilted Octahedra in Perovskites. *Acta Crystallogr. B* **1972**, 28 (11), 3384–3392. <https://doi.org/10.1107/S0567740872007976>.

Supporting Information

Phase Transitions in Low-Dimensional Layered Double Perovskites: The Role of the Organic Moieties

Beatriz Martín-García^{†,‡,}, Davide Spirito^{†,Θ,‡,*}, Giulia Biffi^{†,¶}, Sergey Artyukhin[†], Francesco Bonaccorso^{†,#}, Roman Krahne[†].*

[†]Istituto Italiano di Tecnologia, Via Morego 30, 16163 Genova (Italy)

[‡]CIC nanoGUNE, Tolosa Hiribidea, 76, 20018 Donostia-San Sebastian, Basque Country (Spain)

^ΘIHP–Leibniz-Institut für innovative Mikroelektronik, Im Technologiepark 25, 15236 Frankfurt (Oder) (Germany)

[¶]Dipartimento di Chimica e Chimica Industriale, Università degli Studi di Genova, Via Dodecaneso 31, 16146 Genova (Italy)

[#]BeDimensional S.p.A., via Lungotorrente secca 3d, 16163 Genova (Italy)

Corresponding Authors

*Beatriz Martín-García (b.martingarcia@nanogune.eu) and Davide Spirito (spirito@ihp-microelectronics.com)

Experimental Methods

Synthesis of the materials. The 3D Cs₂AgBiBr₆ crystals were prepared following the recipe from Slavney *et al.*¹ Briefly, BiBr₃ (112.25 mg) and CsBr (106.5 mg) were mixed and dissolved in 2.5 mL of HBr (48% vol.) at 110°C under stirring during 30 min. Then, AgBr (47 mg) was added and under stirring dissolved for 2 h, yielding an orange solution. The slow cooling of this solution to room temperature led to the formation of orange-red crystals, which were isolated by filtration on a Büchner funnel with a fritted glass disc by vacuum suction while washing with acetone. We checked the purity of the crystals by Raman spectroscopy by analyzing the frequency of the A_{1g} mode.² The layered materials were synthesized adapting the recipe from Connor *et al.*³ The (R-NH₃)₄AgBiBr₈ 1L crystals were growth by mixing BiBr₃ (102 mg), AgBr (42.5 mg) and the corresponding organic spacer (PA -75 µL, BA -90 µL, PEA -115 µL, DA-182 µL and DoA-209 µL) in 650 µL of HBr (48% vol) at 100°C under stirring during 30 min. The slow cooling of this yellow solution to room temperature led to the formation of yellow crystals, which were isolated by filtration on a Büchner funnel with a fritted glass disc by vacuum suction while washing with diethyl ether. The (R-NH₃)₂CsAgBiBr₇ 2L crystals were grown by mixing BiBr₃ (75.5 mg), CsBr (36 mg), AgBr (31.5 mg) and the corresponding organic spacer (PA -154 µL, BA -185 µL, PEA -236 µL, DA-374 µL and DoA-430 µL) in 1 mL of HBr (48% vol) at 100°C under stirring during 30 min. The slow cooling of this yellow solution to room temperature led to the formation of yellow-orange crystals, which were isolated by filtration on a Büchner funnel with a fritted glass disc by vacuum suction while washing with acetone. To allow the dissolution of DA and DoA in the reaction medium, 2 mL of toluene were added. All the collected crystals were dried inside a vial overnight (12 h) at room temperature in a Büchi® B-585 drying glass oven.

Optical characterization. The temperature-dependent absorbance spectroscopy was carried out in a Bruker Vertex 80V FT-spectrometer equipped with an Oxford Optistat liquid N₂-cryostat. Absorbance spectra at room temperature were collected using a Varian Cary 5000 UV-Vis-NIR spectrophotometer (Agilent Technologies) and Jasco V730 UV-Vis spectrophotometer. Thin films of the materials were deposited on cleaned quartz substrates (SPI[®] supplies) by spin coating (3000 rpm for 40s and then 5000 rpm for 20s) solutions prepared by dissolving the crystals (~300 mg/mL in DMSO for 3D and 2L and in DMF for 1L) followed by an annealing step at 285°C (5 min)⁴, 135°C (7 min)³ and 100°C (4 min)³ for the 3D, 2L and 1L perovskites, respectively. Prior to the spin coating step, the glass substrates were cleaned in an ultrasonic bath subsequently with acetone and isopropanol (8 min each step), dried under a N₂ flow followed by a final O₂ plasma treatment (120s, 100W).

Photoluminescence spectra were collected with a Horiba i-hr320 spectrometer equipped with a Si CCD, with excitation at 325 nm (power on sample ~0.1 mW), and using a Cassegrain objective (15×, 0.28 NA). All data has been corrected by the spectral response of the system. Temperature-dependent measurements were carried out using a liquid nitrogen cryostat from Linkam[®], with a quartz window for the optical access and emission collection in backscattering configuration.

Raman spectroscopy characterization. Room-temperature Raman measurements were carried out in a Renishaw[®] inVia equipped with a 50× (0.75 N.A.) objective with an excitation wavelength of 532 nm using a laser power < 0.1 mW, to avoid the damage of the samples during the measurement. The temperature-dependent Raman spectroscopy study was performed using a liquid nitrogen cryostat from Linkam[®] mounted in a Renishaw[®] inVia microscope equipped with a long working distance objective (50×, 0.50 NA).

X-ray diffraction characterization. The XRD analysis was carried out using a PANalytical Empyrean X-ray diffractometer, equipped with a 1.8 kW CuK α ceramic X-ray tube and a PIXcel3D 2x2 area detector, operating at 45 kV and 40 mA at room temperature. The crystals were deposited onto a quartz zero-diffraction single crystal substrate for the XRD measurements. The diffraction patterns were collected under ambient conditions using parallel beam geometry and symmetric reflection mode. XRD data analysis was carried out using the HighScore 4.1 software from PANalytical.

Characterization of the materials.

Figure S1 includes a series of optical microscope images of the other samples under study in this work not shown in the main text, highlighting the change in the color of the crystals when replacing Cs⁺ with the alkyl and phenyl ammonium cations.

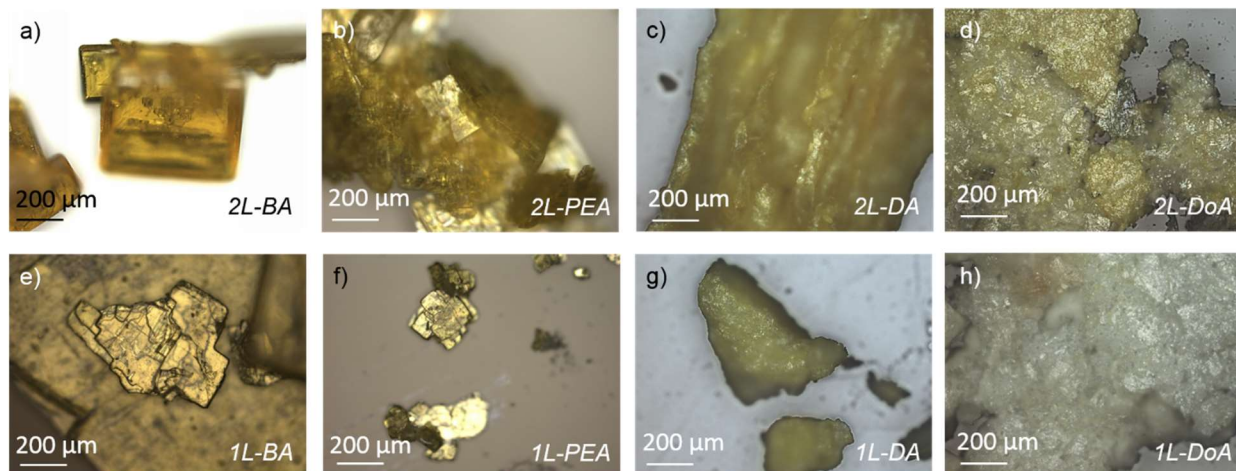


Figure S1. Representative optical microscope images of the resulting crystals for the 2L-BA, 2L-PEA, 2L-DA, 2L-DoA (top); and 1L-BA, 1L-PEA, 1L-DA, 1L-DoA (bottom).

Evaluation of the structure. The X-Ray diffraction patterns of all the samples involved in this study are shown in **Figure S2**. The XRD spectra of the 3D sample (Figure S2a) matches with the patterns described in the reference card (ICSD 291597) for a cubic crystal system ($Fm-3m$

space group) corresponding to the work of McClure *et al.*⁵ When incorporating the organic moieties to form the 2L and 1L systems, this cubic structure evolves to monoclinic (see **Table S1**),^{3,6,7} and some diffraction peaks arising from specific reflections along the $(h\ 0\ 0)$ direction start to appear in the 1L systems. From the periodicity of these diffraction peaks one can estimate the interlayer distance between the octahedral layers (d) displayed in Figure 1h (see main text and **Table S2**) between the $(\text{AgBr}_6)^{5-}$ - $(\text{BiBr}_6)^{3-}$ octahedral layers by applying the Bragg's law [$n\lambda = 2d \sin\theta$], in which $n = 1$ and $\lambda(\text{Cu}) = 1.54 \text{ \AA}$.^{8,9} The d values determined by our XRD measurements agree well with the values estimated from the crystal structures built using Vesta[®] software¹⁰ from the crystallographic data available in literature^{3,6} (using ammonium alkyl chain moieties) concretely for 1L-PA, 1L-BA and 1L-OcA. The corresponding crystal structures show a crossover or entanglement of the alkyl chains when increasing the alkyl chain length (see **Figure S3a**). To visualize the possible arrangement of the organic moieties in 1L-DA and 1L-DoA, we sketched their crystal structures based on the 1L-OcA structure considering the d value obtained from XRD, 23 Å and 20 Å, respectively. As can be observed in Figure S3b, in the case of 1L-DoA a clear crossover of the dodecylammonium moieties should occur, that would explain the shorter d value in comparison with 1L-DA sample. This change in the trend of the interlayer distance is different from the monotonical increasing observed in 2D lead halide perovskites, concretely $(\text{C4-C18})_2\text{PbI}_4$, in which the crystal structure and space group is kept for the whole family of compounds.¹¹⁻¹³ However, in the double $(\text{C3-C8})_4\text{AgBiBr}_8$ perovskites studied the space group changes when the alkyl chain length varies, thus, it is possible to have a different rearrangement of the moieties leading to differences in the interlayer distance trend.

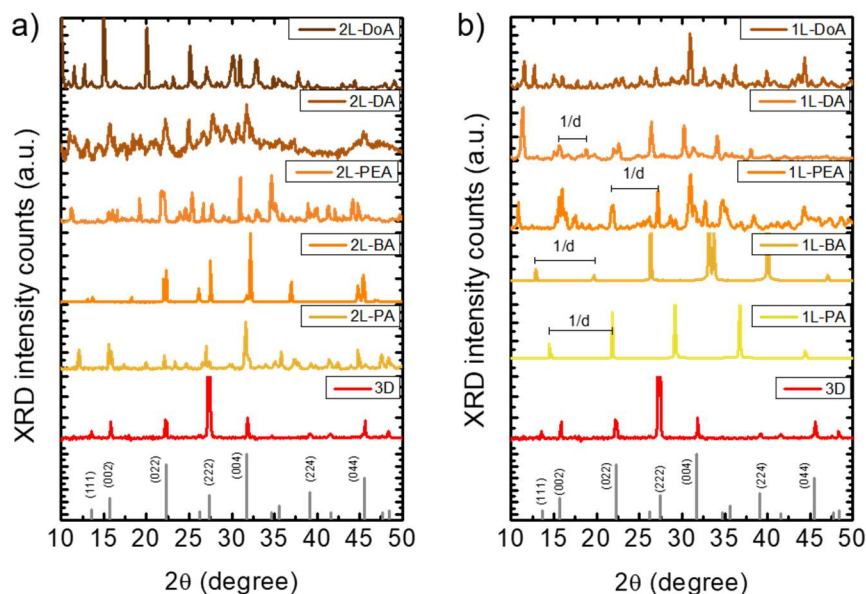


Figure S2. Representative XRD spectra of the synthesized perovskite single crystals: 3D, 2L (a) and 1L (b). The reference pattern (card ICSD 291597) for the 3D sample is also shown.

Table S1. Crystal structures and phase transitions reported in literature $\text{Cs}_2\text{AgBiBr}_6$ crystals and the corresponding layered structures.

Crystal	$T_{\text{transition}}$ (K)	Crystal structure change	Technique(s) of detection	Ref.
3D	122	Tetragonal \rightarrow Cubic	XRD, absorbance, heat capacity	Schade <i>et al.</i> ¹⁴
2L-BA	Between 100 and 298	Monoclinic $P2_1/c \rightarrow$ Monoclinic $C2/m$	XRD	Connor <i>et al.</i> ³
1L-BA	Close to 298	Monoclinic $P2_1 \rightarrow$ Monoclinic $P2_1/m$		
2L-PA	-	? \rightarrow Monoclinic $P2_1/m$	XRD	Mao <i>et al.</i> ⁶
1L-PA	-	? \rightarrow Monoclinic $C2/m$		
1L-OcA	-	? \rightarrow Monoclinic $P2/m$		
1L-BA	-	? \rightarrow Monoclinic $P2_1/m$	XRD	Fang <i>et al.</i> ⁷
2L-PA	222	Monoclinic $P2_1 \rightarrow$ Monoclinic $P2_1/m$	XRD, differential scanning calorimetry	Zhang <i>et al.</i> ¹⁵

Table S2. Evolution of the d parameter obtained from the XRD measurements for the 1L samples using different organic moieties.

Organic moiety	PA	BA	PEA	DA	DoA
Length (Å)	5.5	6.7	8.4	14.3	16.8
1L d (Å)	11±1	12±1	16±2	23±2	20±2

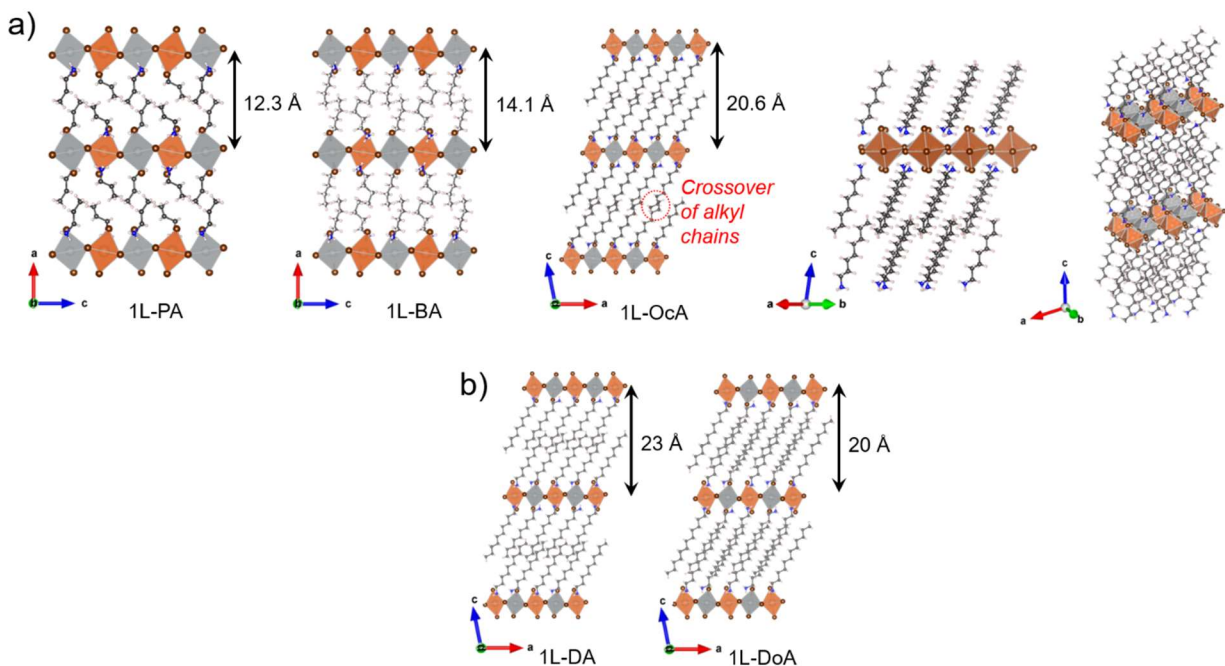


Figure S3. (a) Structure of the 1L-PA, 1L-BA and 1L-OcA crystals at room temperature plotted with VESTA software¹⁰ based on the crystallographic data from refs.^{3,6,7} The distance between the octahedra layers is indicated. (b) Reasonable structures of the 1L-DA and 1L-DoA crystals at room temperature built by VESTA software¹⁰ based on the d values determined by XRD and the crystallographic data from 1L-OcA in ref⁶.

From the crystallographic data available in the literature for 3D,¹⁴ 2L-/1L-PA,⁶ 2L-/1L-BA³ and 1L-OcA⁶ (see Table S1), we quantified the lattice distortion induced by the presence of the corresponding organic molecules by the mean octahedral quadratic elongation parameter (λ_{oct}),¹⁶ following the equation Eq. S1:

$$\lambda_{oct} = \frac{1}{6} \sum_{i=1}^6 \left(\frac{\ell_i}{\ell_0} \right) \quad [\text{Eq. S1}]$$

in which ℓ_0 and ℓ_i are the center (Ag^+ or Bi^{3+})-to-vertex (Br^-) distance in the octahedron, respectively. The center-to-vertex distances have been determined using Vesta[®] software¹⁰ and the crystallographic data reported in refs.^{3,6,7}. In this way, we evaluate the changes in the Ag-Br and

Bi-Br bond lengths with respect to the symmetric octahedron in the 3D crystal (see **Table S3**). Evaluating the λ_{oct} for both Ag and Br-containing octahedra, $(\text{AgBr}_6)^{5-}$ and $(\text{BiBr}_6)^{3-}$, with respect to the 3D, and using PA crystals as a representative example, we obtain: 3D ($\lambda_{\text{Ag-Br}} = \lambda_{\text{Bi-Br}} = 1$), 2L-PA ($\lambda_{\text{Ag-Br}} = 1.022$ and $\lambda_{\text{Bi-Br}} = 1.011$) and 1L-PA ($\lambda_{\text{Ag-Br}} = 1.048$ and $\lambda_{\text{Bi-Br}} = 1.013$). Here, the stronger distortion occurs in the $(\text{AgBr}_6)^{5-}$ octahedron, as was also pointed out by Connor *et al.* for 2L-BA and 1L-BA.³ Comparison with the values of Connor *et al.*³ reveals that the length of the organic spacer also plays a role, since for the BA moieties a stronger distortion is observed: 2L-BA ($\lambda_{\text{Ag-Br}} = 1.034$) and 1L-BA ($\lambda_{\text{Ag-Br}} = 1.072$). The structural data provided by Connor *et al.*³ indicates changes in the octahedral tilt pattern in the inorganic layer with increasing temperature, as shown for the 1L-BA crystal in **Figure S4** (prepared using Vesta[®] software¹⁰), in which the angles between the successive octahedra $(\text{AgBr}_6)^{5-}/(\text{BiBr}_6)^{3-}/(\text{AgBr}_6)^{5-}$ in the same layer defined by the Bi-Br-Ag bonds vary from 186° to 163° when passing from 100 K to 298 K.

Table S3. Ag-Br and Bi-Br bond distortion in terms of the mean octahedral quadratic elongation parameter (λ_{oct}) for the $(\text{AgBr}_6)^{5-}$ and $(\text{BiBr}_6)^{3-}$ octahedra for different organic cations in the 2L and 1L crystals compared to the 3D counterpart.

Crystal	$\lambda_{\text{Ag-Br}}$		$\lambda_{\text{Bi-Br}}$	
	T < T _{transition}	T > T _{transition}	T < T _{transition}	T > T _{transition}
3D	1	1	1	1
2L-PA	-	1.022	-	1.011
1L-PA	-	1.048	-	1.013
2L-BA	1.038	1.034	1.022	1.017
1L-BA	1.058	1.072	1.026	1.017
1L-OcA	-	1.029	-	1.005

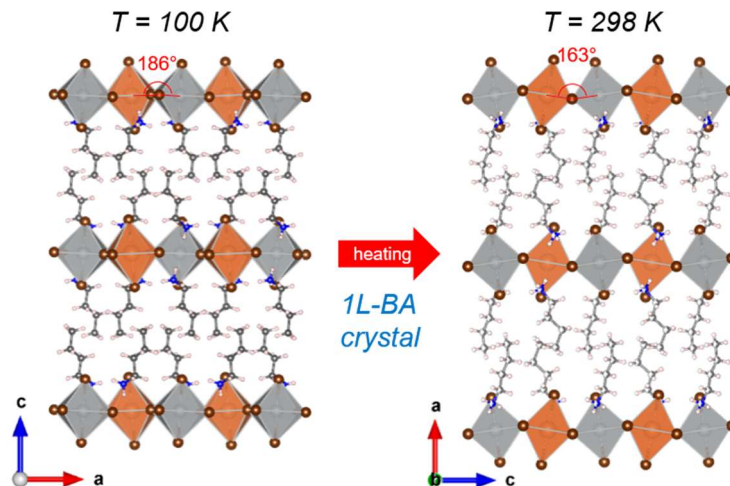


Figure S4. Structure of the 1L-BA crystal at $T = 100\text{K}$ and $T = 298\text{K}$ visualized with VESTA 3 software¹⁰ based on the crystallographic data from ref.³.

Figure S5a-b shows the Raman spectra in the $100\text{-}300\text{ cm}^{-1}$ range at room temperature, which reveal a systematic red shift of the A_{1g} Raman mode, when the system changes from 3D ($176\pm 2\text{ cm}^{-1}$, in agreement with literature^{2,17,18}) to 2L and to 1L materials. Mechanically exfoliated (Scotch tape) 2L or 1L samples on silicon wafers (90 nm thermal SiO_2 , Ti/Au markers defined by direct laser-writer using a DWL 66FS, Heidelberg Instruments Mikrotechnik GmbH) are depicted in Figure S5c, as thin blue-white colored flakes. The observed Raman modes did not show any dependence on the thickness of the flakes, indicating that the position of the Raman modes only depends on the crystal structure, but not on the thickness of the crystal.

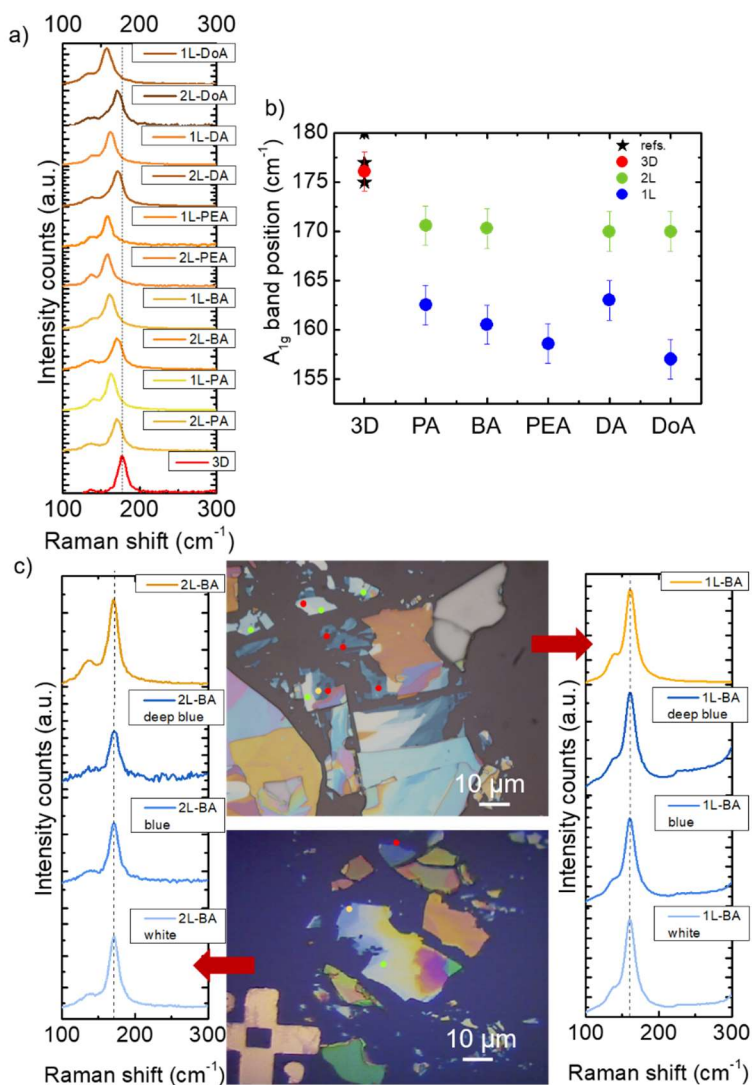


Figure S5. (a) Representative Raman spectra (532 nm excitation wavelength) of the 3D, 2L and 1L crystals in the 100-300 cm⁻¹ range. (b) Position of the A_{1g} mode in the Raman spectrum for the different systems, showing a dependence on the length of the alkyl chain or phenyl group. The star symbols indicate values from the literature for the 3D crystal, refs^{2,17,18}. (c) Raman spectra collected on exfoliated 2L-BA (left graph-bottom image) and 1L-BA (right graph-top image) thin flakes that appear in different colors in the microscope images. The colored dots indicate the measurement spots in the optical microscope images.

Additional Raman spectroscopy data of 3D, PA, BA, PEA, and DA samples

The Raman spectra at different temperatures in the range 80 – 350 K in the 100-250 cm⁻¹ spectral range for the 3D, PA, BA, PEA, and DA samples are shown in (a) panels of **Figures S6-S9**,

respectively. The position and FWHM of the Raman peak associated to the A_{1g} mode is depicted in the (b) panels.

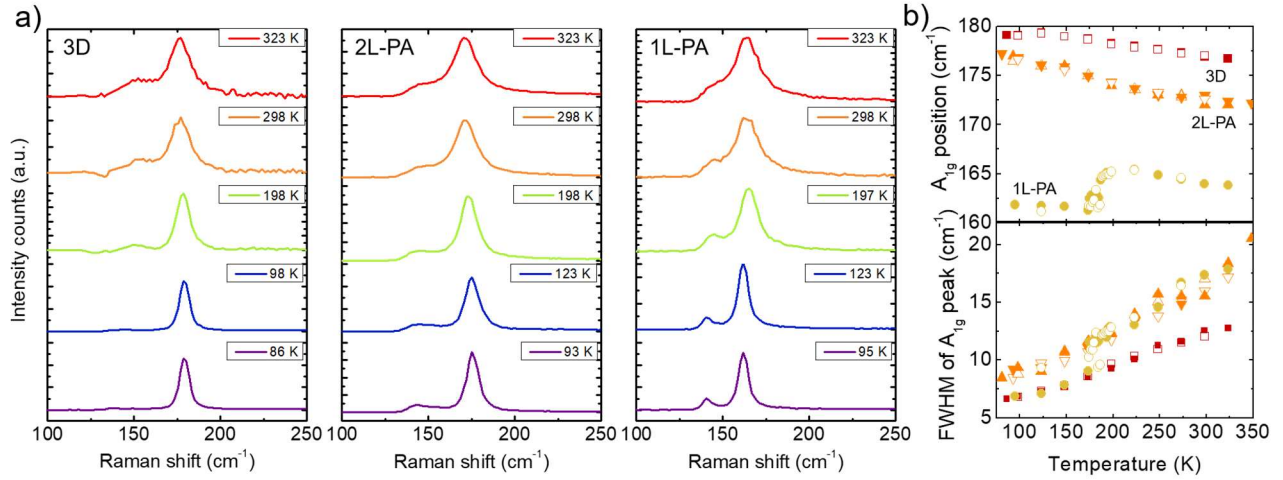


Figure S6. (a) Representative Raman spectra in the $100\text{-}250\text{ cm}^{-1}$ region for 3D, 2L-PA and 1L-PA at selected temperatures, respectively. (b) Temperature evolution of the A_{1g} mode frequency (top panel) and FWHM (bottom panel). Full symbols indicate the data acquired during heating from base temperature, while empty ones during cool down.

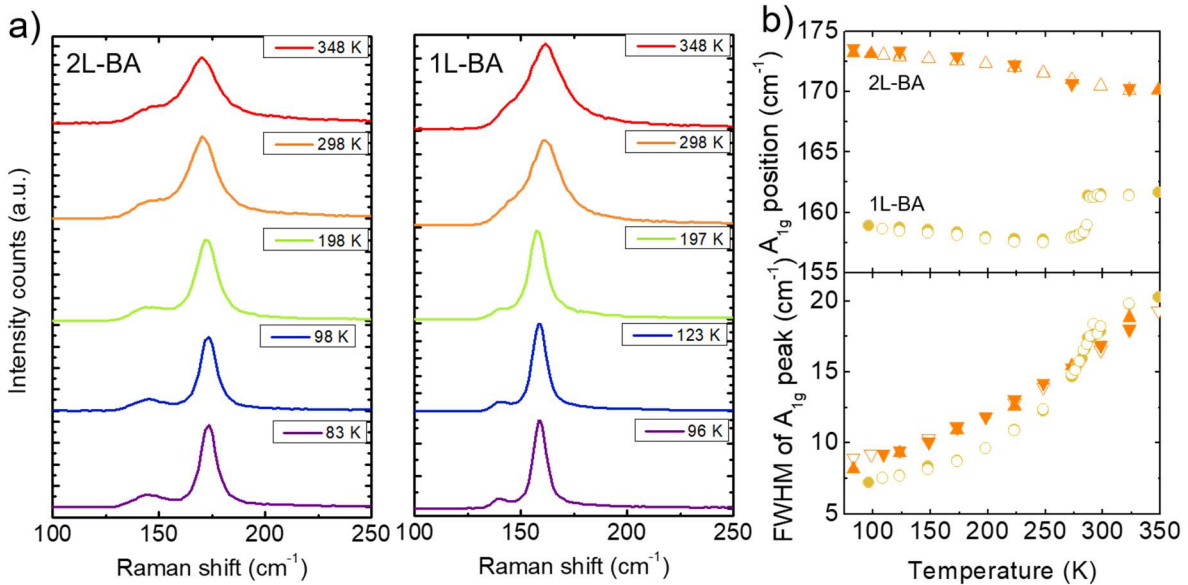


Figure S7. (a) Representative Raman spectra in the $100\text{-}250\text{ cm}^{-1}$ region for 2L-BA and 1L-BA at selected temperatures, respectively. (b) Temperature evolution of the A_{1g} mode frequency (top panel) and FWHM (bottom panel). Full symbols indicate the data acquired during heating from base temperature, while empty ones during cool down.

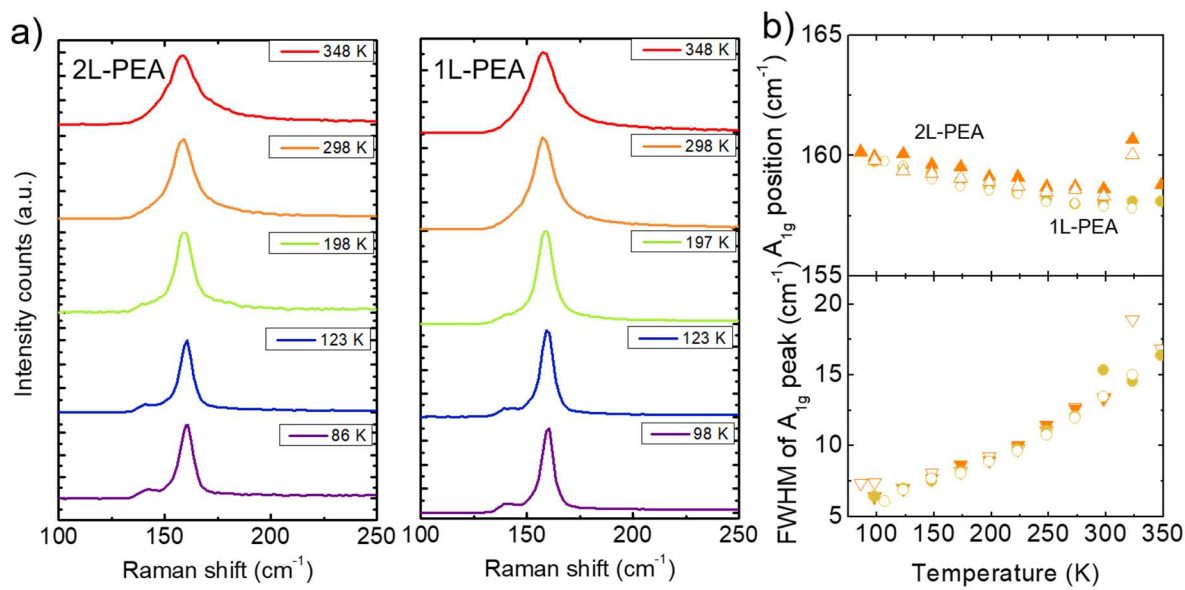


Figure S8. (a) Representative Raman spectra in the 100-250 cm⁻¹ region for 2L-PEA and 1L-PEA at selected temperatures, respectively. (b) Temperature evolution of the A_{1g} mode frequency (top panel) and FWHM (bottom panel). Full symbols indicate the data acquired during heating from base temperature, while empty ones during cool down.

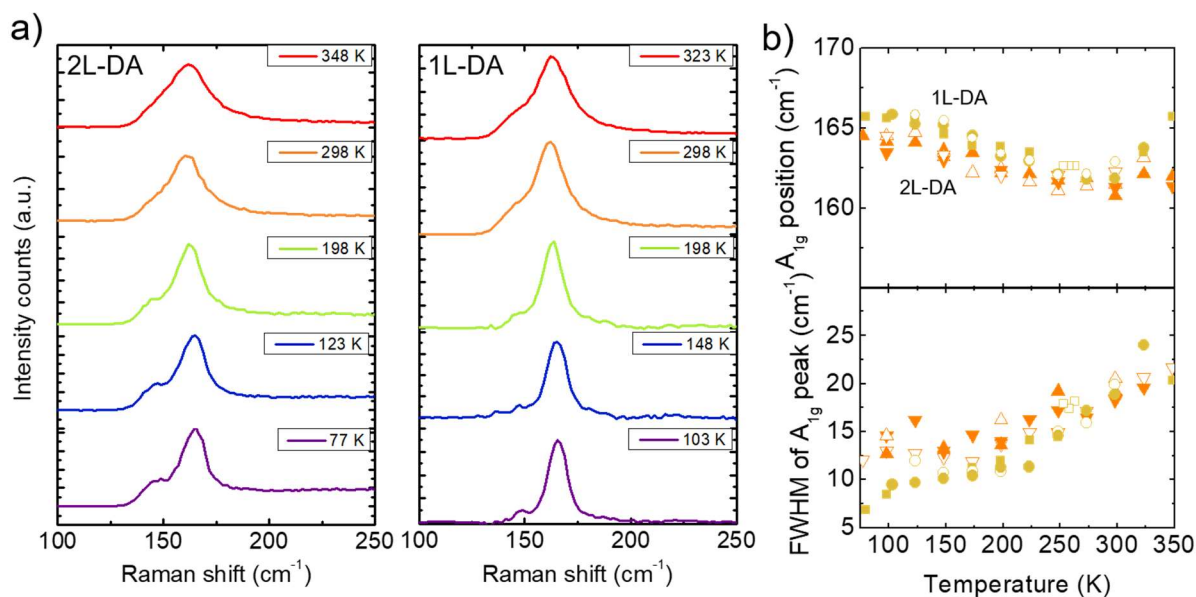


Figure S9. (a) Representative Raman spectra in the 100-250 cm⁻¹ region for 2L-DA and 1L-DA at selected temperatures, respectively. (b) Temperature evolution of the A_{1g} mode frequency (top panel) and FWHM (bottom panel). Full symbols indicate the data acquired during heating from base temperature, while empty ones during cool down.

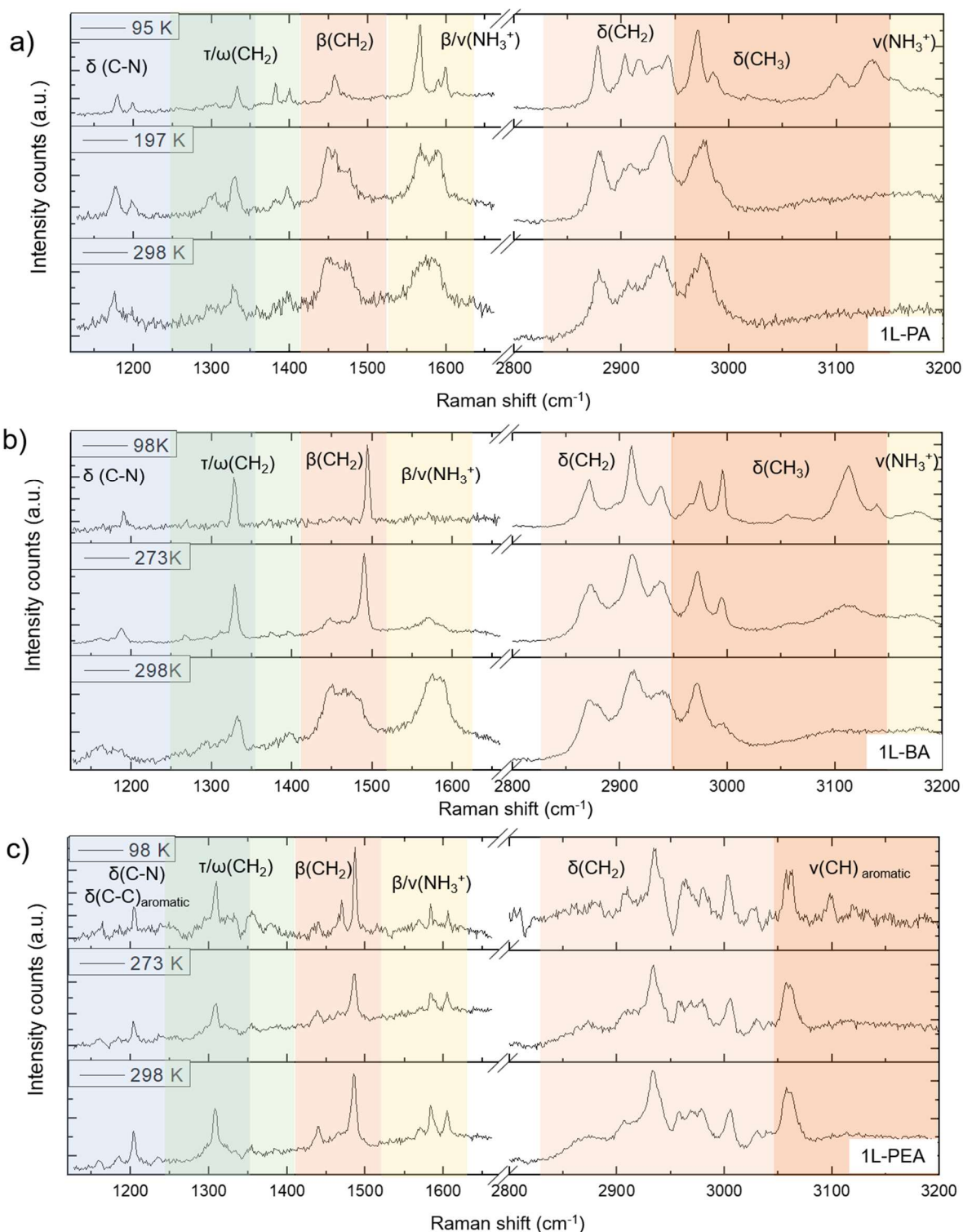


Figure S10. Raman modes of the organic moieties for the 1L systems at different temperature. Representative Raman spectra in the 1100-1650 cm⁻¹ (left) and 2800-3200 cm⁻¹ (right) regions for 1L-PA (a) at selected temperatures: 98, 200 and 298 K; for 1L-BA (b) at 98, 273 and 300 K and 1L-PEA (c) at 98,

200 and 298 K, showing the vibrational modes of the propylammonium, butylammonium and phenylethylammonium cations, respectively. (c) Notation used: δ , stretching, β , bending; τ , twisting; ω , wagging, and ν , other vibrations.

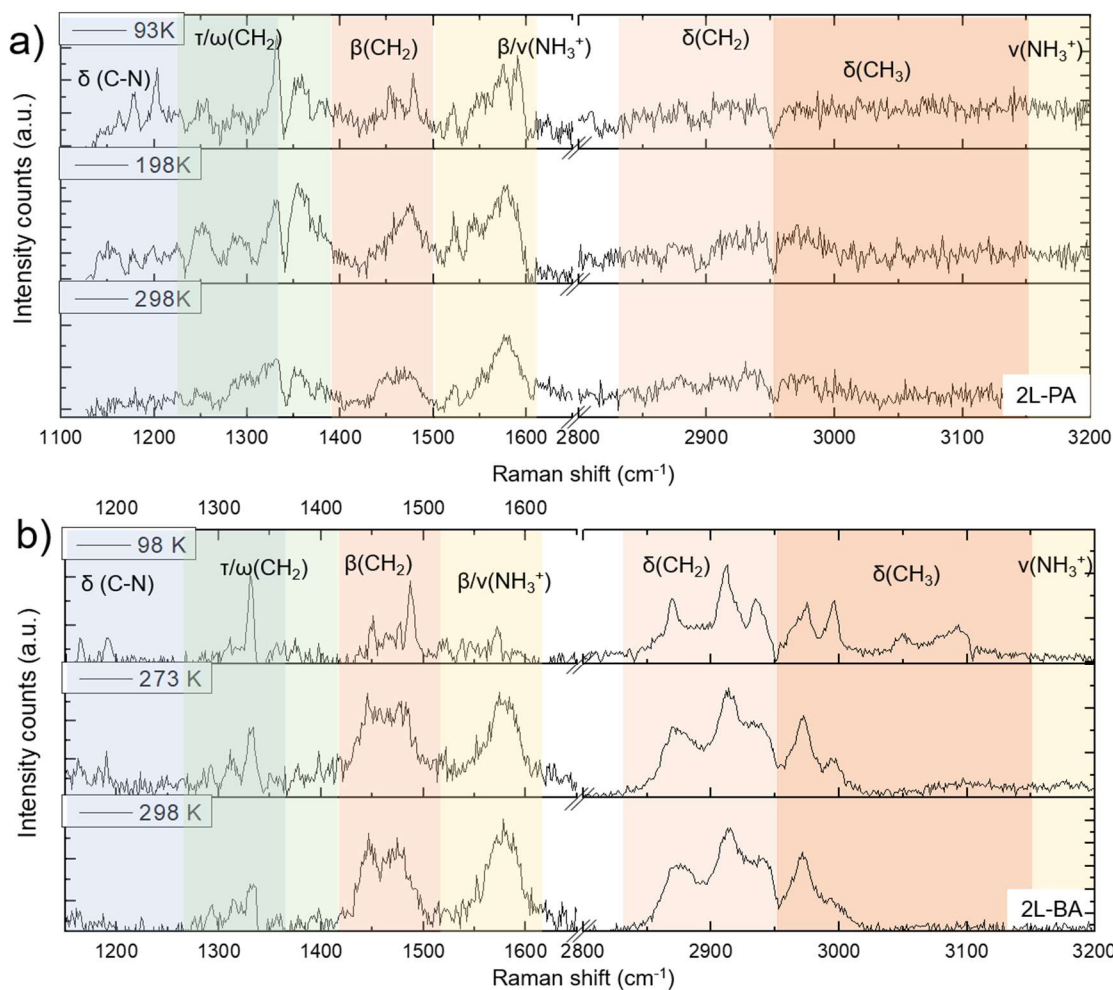


Figure S11. Raman modes of the organic moieties for the PA and BA 2L systems at different temperature. Representative Raman spectra in the 1100-1650 cm⁻¹ (left) and 2800-3200 cm⁻¹ (right) regions for 2L-PA (a) at selected temperatures: 93, 198 and 298 K and for 2L-BA (b) at 98, 273 and 298 K, showing the vibrational modes of the propylammonium and butylammonium cations, respectively. Notation used: δ , stretching, β , bending; τ , twisting; ω , wagging, and ν , other vibrations.

Additional absorbance and photoluminescence spectroscopy characterization

As in the graphs shown in the main text for 3D and 2L/1L-PA (Figure 4a), in the absorbance spectra of the films prepared from the 2L/1L-BA and 2L/1L-PEA systems, only a slight absorption peak broadening with increasing temperature is observed, see **Figure S12**.

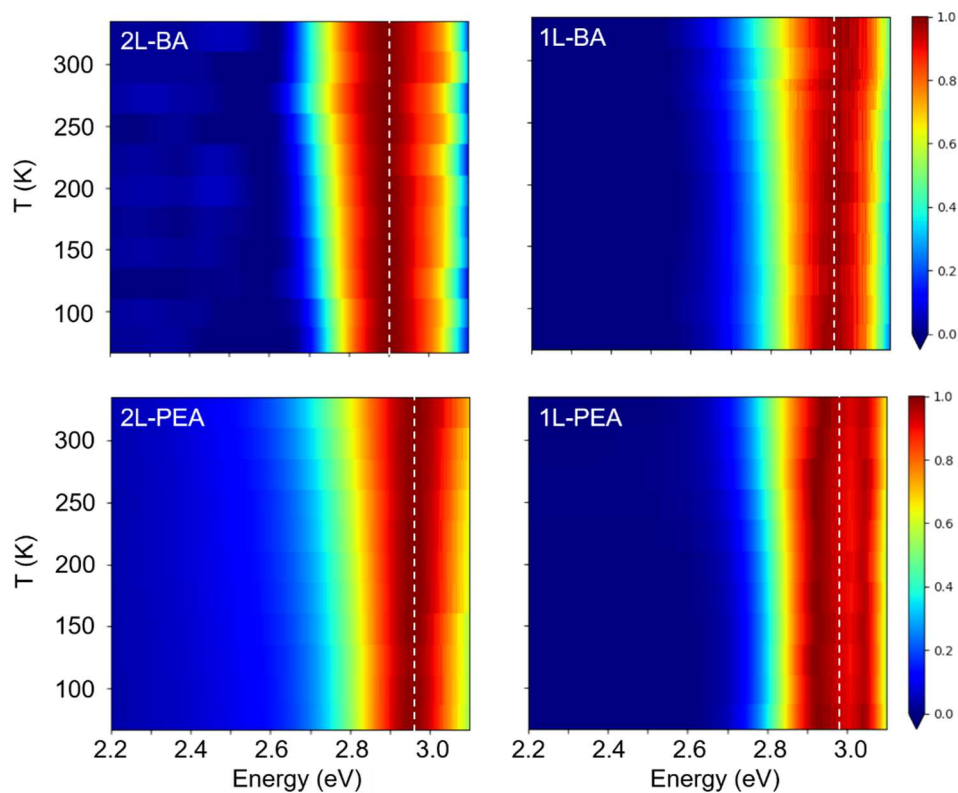


Figure S12. Normalized temperature-dependent absorbance spectra intensity maps for 2L/1L-BA and 2L/1L-PEA films. The dashed line indicates the absorption peak position.

However, in the absorbance spectra at room temperature, displayed in **Figure S13**, a systematic blue shift in the absorption peak position is observed when replacing the Cs^+ with the alkyl and/or phenyl ammonium cations in the $\text{Cs}_2\text{AgBiBr}_6$ perovskite structure towards 2L or 1L together with the organic spacer length, from 3D (2.84 eV, 436 nm) to 2L (2.92 eV, 425 nm) to 1L (2.99 eV, 415 nm) in line with published results³. Therefore, the structural change from 3D to 2L or 1L is also highlighted in the optical properties of the material.

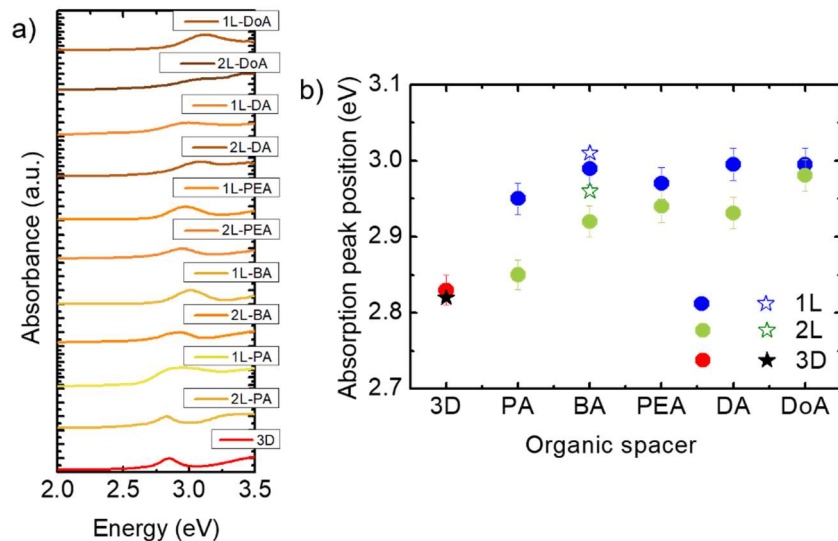


Figure S13. (a) Representative absorbance spectra of the films prepared from the synthesized perovskite single crystals: 3D, 2L and 1L. (b) Absorption peak position change with the introduction of the organic spacer in the perovskite structure. Average values from 3 different films for each sample. For comparison, values from the literature, ref³ are included as star symbols.

Urbach tail analysis of the absorption coefficient slope: We carried out a linear fit of the logarithmic of the absorption coefficient (α) with the photon energy (E) in the range of temperatures (T) under study by means the Urbach rule: $\alpha(E) = \alpha_0 e^{\left(-\sigma \frac{E_0 - E}{k_B T}\right)}$; concretely $\ln(\alpha)$ vs E , see **Figure S14**, to determine if the linear fits converge to a single point corresponding to (E_0, α_0) that allows to estimate the optical bandgap (see **Table S4** for the values, when crossing, namely at high temperatures).^{3,19,20} We obtain similar results for the optical bandgap from this analysis of the temperature-dependent absorption coefficient and directly from the peak position in the absorption.

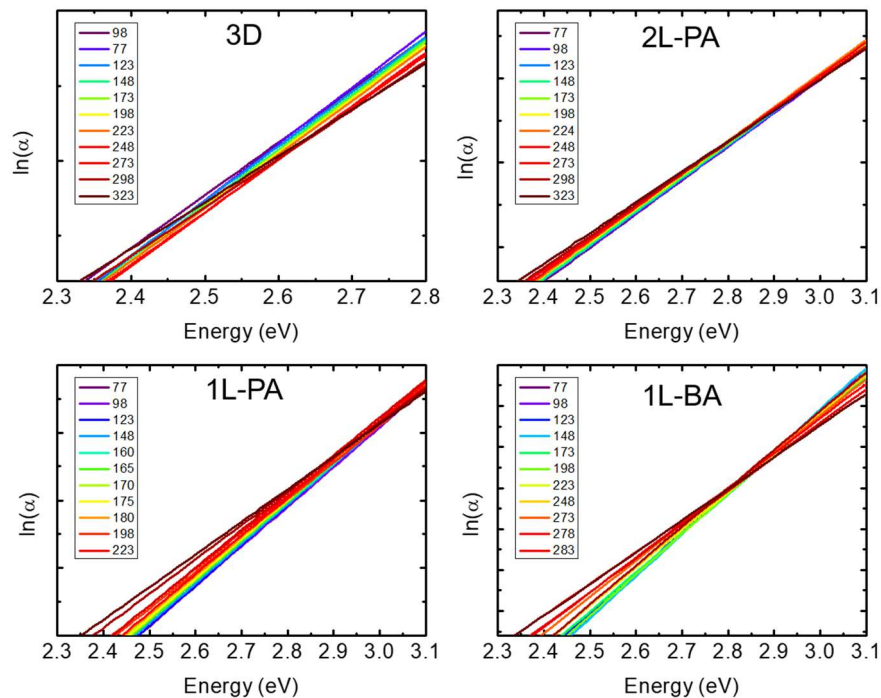


Figure S14. Representative examples of the linear fit obtained from the analysis of the logarithmic of the absorption coefficient (α) with the photon energy (E) for the following samples: 3D, 2L/1L-PA and 1L-BA.

Table S4. Values of the estimated optical bandgap by Urbach tail analysis for several samples.

<i>Sample</i>	<i>abs peak (eV)</i>	<i>E_0 (eV)</i>	<i>crossing above T (K)</i>
3D	2.83	2.65	248
2L-PA	2.85	2.70	248
2L-BA	2.92	3.15	248
2L-PEA	2.94	2.80	248
1L-PA	2.95	2.90	223
1L-BA	2.99	2.83	288
1L-PEA	2.97	2.85	248

Complementary PL data: Representative temperature dependent PL spectra for 2L/1L-BA and 2L/1L-PEA samples is shown in **Figures S15-S16**.

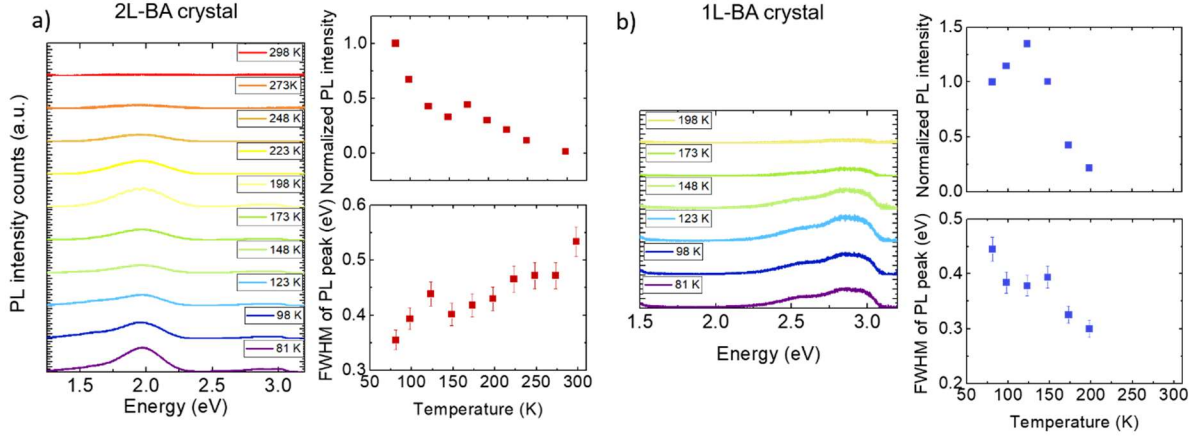


Figure S15. Representative photoluminescence spectra together with the evolution of the PL peak intensity and FWHM for 2L-BA (a) and 1L-BA (b) in the 80 – 350 K range.

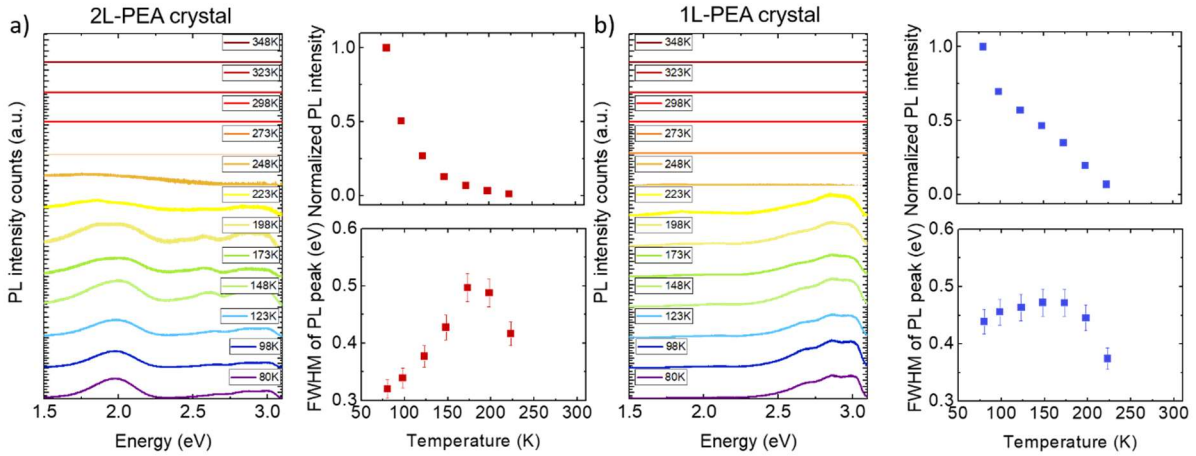


Figure S16. Representative photoluminescence spectra together with the evolution of the PL peak intensity and FWHM for 2L-PEA (a) and 1L-PEA (b) in the 80 – 350 K range.

Evaluation of the electron-phonon coupling and Stokes shift. Another important aspect to evaluate combining the information from Raman spectroscopy and the optical properties of the crystals is the interaction between phonon modes and optical centers, which can be characterized by the Huang-Rhys factor (S)^{2,17}. This factor relates the Stokes shift energy (ΔE_{Stokes}) and the LO phonon energy ($\hbar\omega_{LO}$, in our case related to A_{1g} mode) as $\Delta E_{Stokes} = 2S \hbar\omega_{LO}$. In **Table S5** we summarize the values for absorption peaks (E_{abs}) and PL peaks (E_{PL}) that are almost constant in

the temperature range investigated (80-350K), Raman modes ($\hbar\omega_{LO}$) at low (80K) and room temperature, and evaluate the ($\Delta E_{Stokes}=E_{PL}-E_{abs}$) and the Huang-Rhys parameter $S=\Delta E_{Stokes}/(2\hbar\omega_{LO})$ for the samples used in the PL study. We obtained large Huang-Rhys values for 3D ($S \sim 19$, in line with reported data: 12 for Zelewski *et al.*¹⁷ – 15.4 for Steele *et al.*²) and 2L crystals ($S \sim 22$), confirming strong electron-phonon interactions, while small values for the 1L crystals ($S \sim 1$) were obtained, in accordance with a direct bandgap.

Table S5. Values of the Huang-Rhys factor obtained at 80 K and RT from the absorption, PL peak and Stokes shift for several samples.

<i>Sample</i>	<i>abs peak (eV)</i>	<i>PL peak (eV)</i>	<i>Raman @ 80K (eV)</i>	<i>Raman @ RT (eV)</i>	<i>Stokes shift (eV)</i>	<i>Huang-Rhys factor, S @ 80K</i>	<i>Huang-Rhys factor, S @ RT</i>
3D	2.83	1.97	0.0222	0.0218	0.86	19.4	19.7
2L-PA	2.85	2.04	0.0218	0.0212	0.81	18.6	19.1
2L-BA	2.92	1.98	0.0215	0.0211	0.94	21.9	22.3
2L-PEA	2.94	1.99	0.0199	0.0197	0.95	23.9	24.1
1L-PA	2.95	2.93	0.0201	0.0202	0.02	0.5	0.5
1L-BA	2.99	2.93	0.0197	0.0200	0.06	1.5	1.5
1L-PEA	2.97	3.00	0.0198	0.0197	0	0	0

Computational details

First-principles calculations have been carried out using SIESTA²¹ and Quantum Espresso²² codes with PBEsol exchange-correlation functional²³ and relativistic optimized norm-conserving Vanderbilt (ONCV) pseudopotentials generated by D. Hamann’s code²⁴ and available at pseudo-DOJO²⁵. Crystallographic structures of both BA- and PA-based compounds with single (1L) and double (2L) inorganic layers were retrieved from literature,^{3,6} as well as the crystal structures below and above the transition temperature for BA-based crystals³. For the cases in which multiple orientations of organic moieties were reported, we have only retained one of them and performed a structural optimization of the molecules. We kept the unit cell geometry and inorganic ions fixed, to make sure that the optimization of the alkyl chain conformation does not affect the octahedral

tilt pattern in the inorganic layers. All the simulations have been carried out using the SIESTA code,²¹ and including spin-orbit coupling. Reference calculations with a plane-wave code (Quantum Espresso²²) were performed to validate the basis set and convergence parameters used in SIESTA. Inclusion of spin-orbit coupling (SOC) is of utmost importance to reproduce the band structure, due to the presence of Bi³⁺ ions, whose contribution dominates the lowest conduction bands. If spin-orbit coupling is neglected, the 1 eV splitting of the lowest conduction bands is not captured (**Figure S17a,b**).

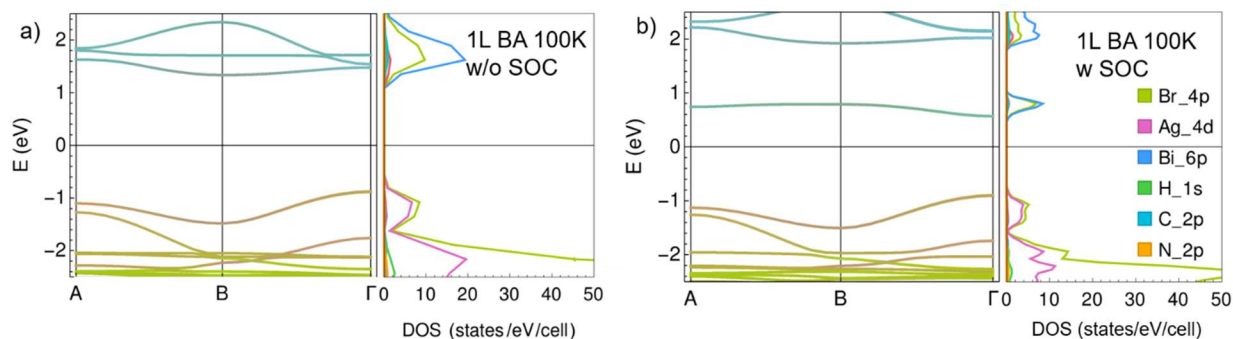


Figure S17. Band structure and projected density of states of (a) 1L-BA at 100K without spin-orbit coupling and (b) 1L-BA at 100K with spin orbit coupling (also shown in Figure 5a of the main text). The inclusion of the spin-orbit coupling turns the indirect bandgap into a direct one for 1L compounds

In the main text, we provided the comparison between 1L-BA and 1L-PA, that shows no major differences in their band structures in the room-temperature structures. Similarly, no major differences are present between the band structures of 2L-BA and 2L-PA (**Figure S18a, b**), further suggesting that while a variation in the organic chain length might affect the transition temperature, it does not considerably influence the bands across the gap and the optical properties of these compounds. Consistently with ref.³, the bandgap is indirect in 2L samples.

For completeness, the study of the electronic properties at different temperatures was performed also on 2L-BA. The results are similar to those reported for the 1L structures, in agreement with the experimental data (Figure S18a, Figure 5b in the main text).

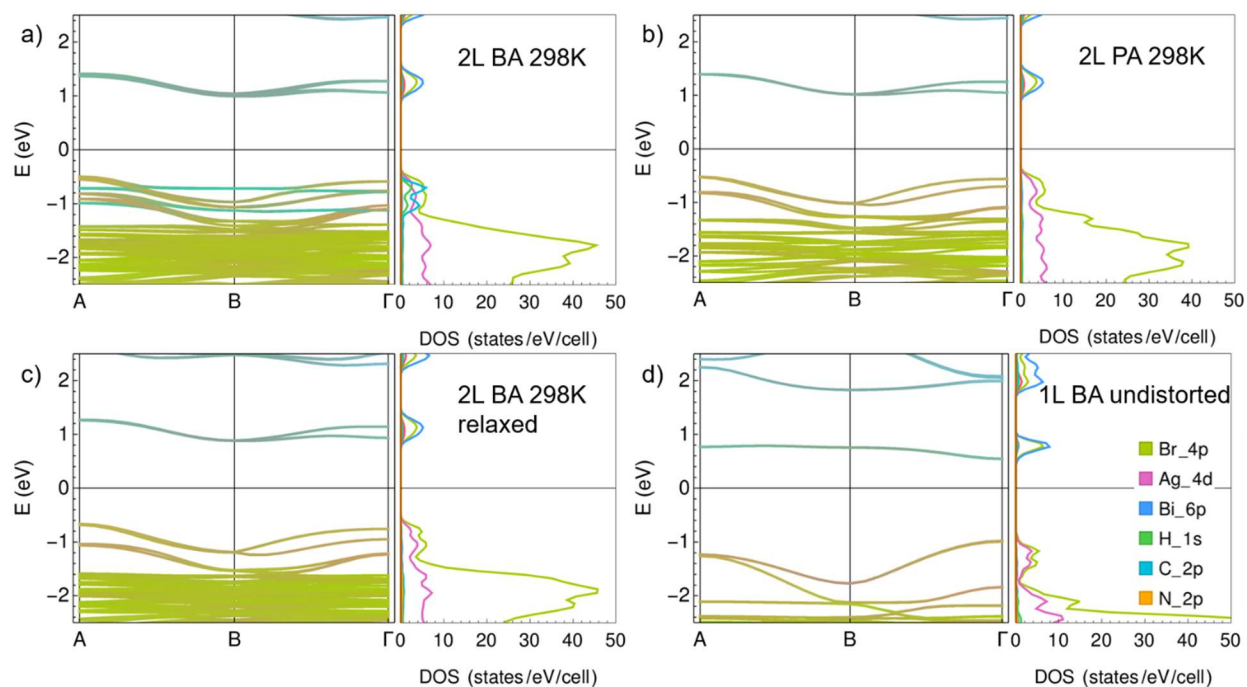


Figure S18. Band structure and projected density of states of (a) 2L-BA at 298K, (b) 2L-PA at 298K, (c) 2L-BA at 298K after geometry relaxation and (d) 1L-BA with undistorted octahedra.

The band structure computed using 2L-BA room temperature structure (with one particular molecular conformation chosen out of multiple atomic positions given in ref.³) without geometry relaxation shows a flat band originating from carbon $2p$ -orbitals intersecting the top valence band. Geometry optimization moves this flat band to lower energies, suggesting this band to be an artefact due to the molecular geometry taken arbitrarily from multiple average positions in the room temperature XRD, being far from the equilibrium conformation of the chain itself (**Figure S18c**). **Figure S18d** shows the band structure and the density of states (DOS) computed for a fictitious structure with octahedral tilts removed: band degeneracies appear at the Brillouin zone boundary in line with the higher symmetry, but the bands across the gap are largely similar to the ones computed using experimental structures. The symmetry of this structure is $Cmmm$ (#65 in International Tables²⁶). The flatness of the conduction band can lead to very interesting phenomena: for example, applying a ferroelectric mode, such as Γ_2^+ , with amplitude as small as

1:10 of that of Γ_3^+ , the one already present at room temperature that causes the out-of-plane tilting of the octahedra, produces a shift in the position of the minimum of the conduction band, thus making the bandgap indirect (**Figure S19b**).

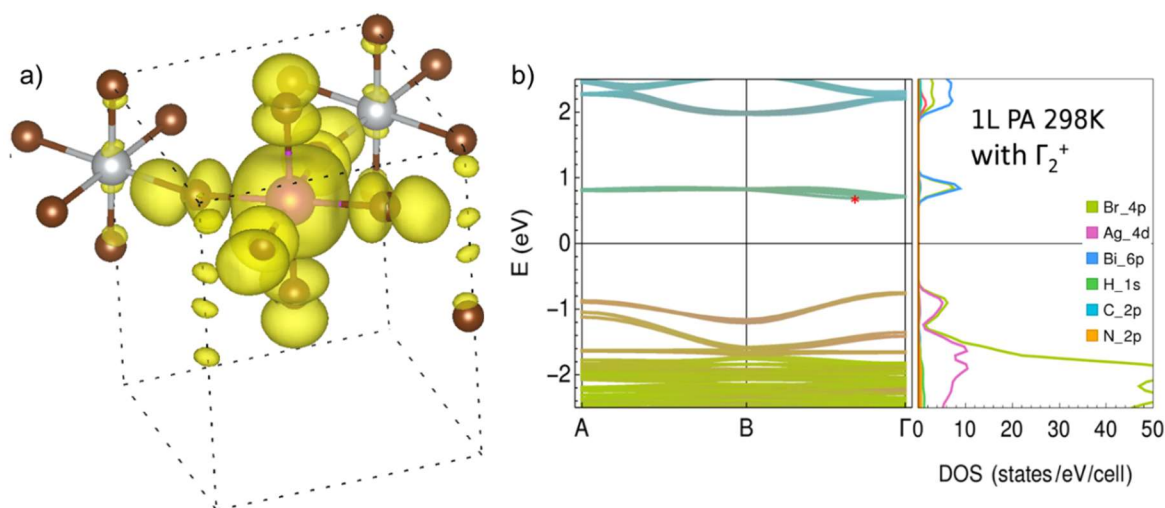


Figure S19. (a) Density of the Bi-centered Wannier function for the lowest conduction band of 1L-BA at low-temperature that does not hybridize with high energy Ag orbitals, resulting in a wavefunction localization on Bi and Br atoms and a flat conduction band. (b) Band structure and projected density of states of the 1L-PA structure at room temperature with a small ferroelectric Γ_2^+ mode applied. The red asterisk marks the minimum of the conduction band.

References:

- (1) Slavney, A. H.; Hu, T.; Lindenberg, A. M.; Karunadasa, H. I. A Bismuth-Halide Double Perovskite with Long Carrier Recombination Lifetime for Photovoltaic Applications. *J. Am. Chem. Soc.* **2016**, *138* (7), 2138–2141. <https://doi.org/10.1021/jacs.5b13294>.
- (2) Steele, J. A.; Puech, P.; Keshavarz, M.; Yang, R.; Banerjee, S.; Debroye, E.; Kim, C. W.; Yuan, H.; Heo, N. H.; Vanacken, J.; et al. Giant Electron–Phonon Coupling and Deep Conduction Band Resonance in Metal Halide Double Perovskite. *ACS Nano* **2018**, *12* (8), 8081–8090. <https://doi.org/10.1021/acsnano.8b02936>.
- (3) Connor, B. A.; Leppert, L.; Smith, M. D.; Neaton, J. B.; Karunadasa, H. I. Layered Halide Double Perovskites: Dimensional Reduction of $\text{Cs}_2\text{AgBiBr}_6$. *J. Am. Chem. Soc.* **2018**, *140* (15), 5235–5240. <https://doi.org/10.1021/jacs.8b01543>.
- (4) Greul, E.; Petrus, M. L.; Binek, A.; Docampo, P.; Bein, T. Highly Stable, Phase Pure $\text{Cs}_2\text{AgBiBr}_6$ Double Perovskite Thin Films for Optoelectronic Applications. *J. Mater. Chem. A* **2017**, *5* (37), 19972–19981. <https://doi.org/10.1039/C7TA06816F>.

- (5) McClure, E. T.; Ball, M. R.; Windl, W.; Woodward, P. M. Cs₂AgBiX₆ (X = Br, Cl): New Visible Light Absorbing, Lead-Free Halide Perovskite Semiconductors. *Chem. Mater.* **2016**, *28* (5), 1348–1354. <https://doi.org/10.1021/acs.chemmater.5b04231>.
- (6) Mao, L.; Teicher, S. M. L.; Stoumpos, C. C.; Kennard, R. M.; DeCrescent, R. A.; Wu, G.; Schuller, J. A.; Chabynyc, M. L.; Cheetham, A. K.; Seshadri, R. Chemical and Structural Diversity of Hybrid Layered Double Perovskite Halides. *J. Am. Chem. Soc.* **2019**, *141* (48), 19099–19109. <https://doi.org/10.1021/jacs.9b09945>.
- (7) Fang, Y.; Zhang, L.; Wu, L.; Yan, J.; Lin, Y.; Wang, K.; Mao, W. L.; Zou, B. Pressure-Induced Emission (PIE) and Phase Transition of a Two-dimensional Halide Double Perovskite (BA)₄AgBiBr₈ (BA=CH₃(CH₂)₃NH₃⁺). *Angew. Chem. Int. Ed.* **2019**, *58* (43), 15249–15253. <https://doi.org/10.1002/anie.201906311>.
- (8) Dhanabalan, B.; Castelli, A.; Palei, M.; Spirito, D.; Manna, L.; Krahne, R.; Arciniegas, M. Simple Fabrication of Layered Halide Perovskite Platelets and Enhanced Photoluminescence from Mechanically Exfoliated Flakes. *Nanoscale* **2019**, *11* (17), 8334–8342. <https://doi.org/10.1039/C9NR00638A>.
- (9) Castelli, A.; Biffi, G.; Ceseracciu, L.; Spirito, D.; Prato, M.; Altamura, D.; Giannini, C.; Artyukhin, S.; Krahne, R.; Manna, L.; et al. Revealing Photoluminescence Modulation from Layered Halide Perovskite Microcrystals upon Cyclic Compression. *Adv. Mater.* **2019**, *31* (1), 1805608. <https://doi.org/10.1002/adma.201805608>.
- (10) Momma, K.; Izumi, F. VESTA 3 for Three-Dimensional Visualization of Crystal, Volumetric and Morphology Data. *J. Appl. Crystallogr.* **2011**, *44* (6), 1272–1276. <https://doi.org/10.1107/S0021889811038970>.
- (11) Billing, D. G.; Lemmerer, A. Synthesis, Characterization and Phase Transitions in the Inorganic–Organic Layered Perovskite-Type Hybrids [(C_nH_{2n+1}NH₃)₂PbI₄], n = 4, 5 and 6. *Acta Crystallogr. Sect. B* **2007**, *63* (5), 735–747.
- (12) Billing, D. G.; Lemmerer, A. Synthesis, Characterization and Phase Transitions of the Inorganic–Organic Layered Perovskite-Type Hybrids [(C_nH_{2n+1}NH₃)₂PbI₄] (n = 12, 14, 16 and 18). *New J. Chem.* **2008**, *32* (10), 1736. <https://doi.org/10.1039/b805417g>.
- (13) Lemmerer, A.; Billing, D. G. Synthesis, Characterization and Phase Transitions of the Inorganic–Organic Layered Perovskite-Type Hybrids [(C_nH_{2n+1}NH₃)₂PbI₄], n = 7, 8, 9 and 10. *Dalton Trans* **2012**, *41* (4), 1146–1157. <https://doi.org/10.1039/C0DT01805H>.
- (14) Schade, L.; Wright, A. D.; Johnson, R. D.; Dollmann, M.; Wenger, B.; Nayak, P. K.; Prabhakaran, D.; Herz, L. M.; Nicholas, R.; Snaith, H. J.; et al. Structural and Optical Properties of Cs₂AgBiBr₆ Double Perovskite. *ACS Energy Lett.* **2019**, *4* (1), 299–305. <https://doi.org/10.1021/acsenergylett.8b02090>.
- (15) Zhang, W.; Hong, M.; Luo, J. Halide Double Perovskite Ferroelectrics. *Angew. Chem. Int. Ed.* **2020**, *59* (24), 9305–9308. <https://doi.org/10.1002/anie.201916254>.
- (16) Robinson, K.; Gibbs, G. V.; Ribbe, P. H. Quadratic Elongation: A Quantitative Measure of Distortion in Coordination Polyhedra. *Science* **1971**, *172* (3983), 567–570. <https://doi.org/10.1126/science.172.3983.567>.
- (17) Zelewski, S. J.; Urban, J. M.; Surrente, A.; Maude, D. K.; Kuc, A.; Schade, L.; Johnson, R. D.; Dollmann, M.; Nayak, P. K.; Snaith, H. J.; et al. Revealing the Nature of Photoluminescence Emission in the Metal–Halide Double Perovskite Cs₂AgBiBr₆. *J. Mater. Chem. C* **2019**, *7* (27), 8350–8356. <https://doi.org/10.1039/C9TC02402F>.
- (18) Kentsch, R.; Scholz, M.; Horn, J.; Schlettwein, D.; Oum, K.; Lenzer, T. Exciton Dynamics and Electron–Phonon Coupling Affect the Photovoltaic Performance of the Cs₂AgBiBr₆

- Double Perovskite. *J. Phys. Chem. C* **2018**, *122* (45), 25940–25947. <https://doi.org/10.1021/acs.jpcc.8b09911>.
- (19) Kurik, M. V. Urbach Rule. *Phys. Status Solidi A* **1971**, *8* (1), 9–45. <https://doi.org/10.1002/pssa.2210080102>.
- (20) Tang, H.; Lévy, F.; Berger, H.; Schmid, P. E. Urbach Tail of Anatase TiO₂. *Phys. Rev. B* **1995**, *52* (11), 7771–7774. <https://doi.org/10.1103/PhysRevB.52.7771>.
- (21) Soler, J. M.; Artacho, E.; Gale, J. D.; García, A.; Junquera, J.; Ordejón, P.; Sánchez-Portal, D. The SIESTA Method for *Ab Initio* Order- *N* Materials Simulation. *J. Phys. Condens. Matter* **2002**, *14* (11), 2745–2779. <https://doi.org/10.1088/0953-8984/14/11/302>.
- (22) Giannozzi, P.; Baroni, S.; Bonini, N.; Calandra, M.; Car, R.; Cavazzoni, C.; Ceresoli, D.; Chiarotti, G. L.; Cococcioni, M.; Dabo, I.; et al. QUANTUM ESPRESSO: A Modular and Open-Source Software Project for Quantum Simulations of Materials. *J. Phys. Condens. Matter* **2009**, *21* (39), 395502. <https://doi.org/10.1088/0953-8984/21/39/395502>.
- (23) Perdew, J. P.; Ruzsinszky, A.; Csonka, G. I.; Vydrov, O. A.; Scuseria, G. E.; Constantin, L. A.; Zhou, X.; Burke, K. Restoring the Density-Gradient Expansion for Exchange in Solids and Surfaces. *Phys. Rev. Lett.* **2008**, *100* (13), 136406. <https://doi.org/10.1103/PhysRevLett.100.136406>.
- (24) Hamann, D. R. Optimized Norm-Conserving Vanderbilt Pseudopotentials. *Phys. Rev. B* **2013**, *88* (8), 085117. <https://doi.org/10.1103/PhysRevB.88.085117>.
- (25) Schlipf, M.; Gygi, F. Optimization Algorithm for the Generation of ONCV Pseudopotentials. *Comput. Phys. Commun.* **2015**, *196*, 36–44. <https://doi.org/10.1016/j.cpc.2015.05.011>.
- (26) Aroyo, M. I.; Perez-Mato, J. M.; Capillas, C.; Kroumova, E.; Ivantchev, S.; Madariaga, G.; Kirov, A.; Wondratschek, H. Bilbao Crystallographic Server: I. Databases and Crystallographic Computing Programs. *Z. Für Krist. - Cryst. Mater.* **2006**, *221* (1). <https://doi.org/10.1524/zkri.2006.221.1.15>.